To the Graduate Council:

I am submitting herewith a thesis written by Brent W. Blaha entitled "A Holographic Reconstruction System for Measuring Concentration Profiles in an Alloy Metal Model Under Directional Solidification." I have examined the final copy of this thesis for form and content and recommend that it be accepted in partial fulfillment of the requirements for the degree of Master of Science, with a major in Mechanical Engineering.

Dwayne McCay

T. Dwayne McCay, Major Professor

We have read this thesis
and recommend its acceptance:

Mary Helen McCay

L. Montgomery Smith

John A. Hopkins

Accepted for the Council:

C W Minkel

Associate Vice Chancellor and
Dean of the Graduate School

STATEMENT OF PERMISSION TO USE

In presenting this thesis in partial fulfillment of the requirements for a Master's degree at the University of Tennessee, Knoxville, I agree that the library shall make it available to borrowers under rules of the Library. Brief quotations from this thesis are allowable without special permission, provided that accurate acknowledgement of the source is made.

Permission for extensive quotation from or reproduction of this thesis may be granted by my major professor, or in his absence, by the Head of Interlibrary Services when, in the opinion of either, the proposed use of the material is for scholarly purposes. Any copying or use of the material in this thesis for financial gain shall not be allowed without my written permission.

Signature Brent Bell

Date 4/29/94

A HOLOGRAPHIC RECONSTRUCTION SYSTEM FOR MEASURING CONCENTRATION PROFILES IN AN ALLOY METAL MODEL UNDER DIRECTIONAL SOLIDIFICATION

A Thesis

Presented for the

Master of Science

Degree

The University of Tennessee, Knoxville

Brent W. Blaha

May 1994

ACKNOWLEDGEMENTS

I would like to thank those individuals who have assisted me during this research. These include Drs T. Dwayne and Mary Helen McCay, for providing direction and support, and Dr L. Montgomery Smith, for introducing me to the theoretical world of optics; Dr. Bob Owen showed me the finer points of using optics in the laboratory. Dr. John Hopkins has been both a mentor and friend throughout and deserves special recognition as such.

I would like to thank Dave McIntosh and Donnie McGathren and the other guys at HGS for their help with my fellowship and all the support they have given. I also thank Mary Magnani for the use of her thesis and for introducing me to holography. Lastly, but certainly not in the least, I want to thank my wife, Elina, for lifting me when down, turning me when astray, and pushing me when lagging. This would not have been possible without her love and support.

Abstract

The study presented here makes use of holography and interferometry to measure the refractive index and concentration variations within a transparent liquid metal model analogue undergoing directional solidification. Holography is used to record experimental systems under circumstances that prevents the simultaneous application of different optical processing techniques. Interferometry is used to make quantitative measurements of phase changes within the solidification system recorded holographically. Experiments performed under 1 g_e and microgravity conditions are examined.

Holograms were recorded in NASA Marshall Space Flight Center's Holographic Ground System in Huntsville, AL, and in orbit in the space shuttle in NASA's Fluids Experiment System as part of the first International Microgravity Laboratory. Holograms were reconstructed at the University of Tennessee Space Institute and combined with interferometry to produce fringe patterns related to the phase change distribution within the solidification system. Two different procedures for extracting quantitative data from fringe patterns (Fourier transform and intensity) were used and compared.

The results indicate that a well-defined exponential solute distribution forms when solidification is performed without the influence of gravity. With gravity present, the density inversion in the liquid, a result of the solidification process, creates buoyancy driven convection. For this reason, recorded holograms of experiments performed on the ground were taken early in the experiment prior to the onset of convection; the measured

solute distributions are not as well-defined as those measured from experiments performed without gravity applied.

Table of Contents

List of Tables

List of Figures

Nomenclature

English Symbols

a	arbitrary constant field component amplitude
A	constituent A
a(x)	1D background intensity variations
a(x,y)	2D background intensity variations
B	constituent B
b(x)	1D fringe visibility multiplier
b(x,y)	2D fringe visibility multiplier
c	arbitrary constant
C	concentration
C(x)	1D concentration
°C	degrees Centigrade
c(x)	1D coordinate change from b(x)
d	integration length
E	electric Field component
f	focal length
f_0	carrier frequency
I	intensity
I(x)	1D intensity distribution
I(x,y)	2D intensity distribution
k	wave number
L	liquid Phase
M	magnification
mm	millimeter
n	index of refraction
n(x)	1D index of refraction distribution
t	time
T	temperature
x	coordinate in spatial domain
y	coordinate in spatial domain
z	coordinate in spatial domain
$\mathscr{F}$	Fourier transform operator

Greek Symbols

∞	infinity
α	solid phase
β	solid phase
Δ	change in
ψ	electric field component
Ψ	Fourier transform of ψ
ω	frequency of light

ϕ	arbitrary phase
$\phi(x)$	1D phase distribution
$\phi(x,y)$	2D phase distribution
ϕ_0	carrier frequency
λ	wavelength
ν_x	coordinate in frequency domain
ν_y	coordinate in frequency domain
θ	angle between object and reference beams in holographic recording
μ	micro - x 10^{-6}

Subscripts / Superscripts

*	complex conjugate
0	bulk
0	reference
c	carrier
e	eutectic
inc	incident
m	melting
o	object
r	reference

Constants

g_e	1 Earth gravity (9.81 m/s^2)
π	pi $\approx$ 3.1415926
i	imaginary number, $i = (-1)^{1/2}$

Acronyms

CAST	Casting and Solidification Technology
CDG	Central Dark Ground
CLA	Center for Laser Applications
COPS	Confocal Optical Processor System
FES	Fluids Experiment System
GSRP	Graduate Student Researcher's Program
HGS	Holographic Ground System
MSFC	Marshall Space Flight Center
MZI	Mach Zehnder Interferometer
NASA	National Aeronautics and Space Administration
UTSI	University of Tennessee Space Institute

Chapter 1 Introduction

An inexpensive method of manufacturing metal parts is to cast them, where hot liquid material is allowed to cool and solidify in the shape of the vessel containing the metal. Directional solidification, a type of controlled casting, is a method to enhance significantly the material strength and thermal resistance of the finished part for applications where these properties are vital. An example of one such application is the turbine blades used in the space shuttle main engines. The blades are subjected to incredibly high thermal gradients and fuel flow that continuously erode the blades. As the turbine blades are both important to the shuttle and expensive to manufacture, it is desirable to maximize their useable lifespan by making them as resistant to their hostile environment as possible. Directional solidification is one method of doing this.

There are many factors that influence the solidification process, not the least of which is gravity. Various solutal and thermal gradients within the molten metal create the possibility for buoyancy driven convection, which greatly influences the microstructure of the solidifying material. Grain reorientation within the metal can lead to an undesirable defect in the finished cast. For this reason many scientists are examining the basic physical processes involved in directional solidification to gain a better understanding of how materials with higher strength properties can be better produced in the future.

McCay and McCay investigated the influence of gravity by performing solidification experiments aboard the space shuttle in a microgravity environment (McCay and McCay, 1993). They used a transparent metal model analogue to simulate the solidification of actual metal alloy. The various laser optical processing techniques that are typically used to investigate solidification processes (interferometry for example) could not be applied directly to the experiment. Instead, holograms were taken so that the optical processors could be used in a laboratory under more convenient circumstances.

The purpose of this study is to determine concentration profiles within an alloy metal model undergoing directional solidification by applying laser optical processing to reconstructed holograms of the solidifying system. Holograms of the previously mentioned experiments and others were reconstructed in a laboratory and the resulting wavefronts combined in an interferometric optical processor to create fringe patterns. The fringe patterns were then studied using two different fringe pattern analysis schemes to quantitatively determine phase distributions within the laser beam. Finally, phase distributions were converted into concentration distributions by relating phase to index of refraction, which has been experimentally measured as a function of temperature and concentration (McCay et al., 1994).

Recorded holograms of experiments using two different solutions were examined. The first solution, pure water, was used to determine the effects on the index of refraction of the liquid by an applied temperature field. Energy transport was limited to diffusion by aligning the temperature field with gravity such that there was no potential for buoyancy driven convective flow. Aqueous ammonium chloride (NH_4Cl-H_2O) was the second solution studied and showed the application of this method by extracting concentration profiles from an NH_4Cl-H_2O solution under directional solidification in both 1 g_e and μg_e environments.

Each object image wavefront recorded in the holograms was reconstructed in the laboratory and combined with a reference wavefront to form a fringe pattern, which was digitized on an image processor. Two different fringe pattern analysis techniques (Fourier transform and intensity) were applied to the fringe patterns to determine refractive index and concentration profiles within the ammonium chloride solution. The profiles that were produced closely resemble what was expected; an exponentially decreasing concentration distribution and an index of refraction profile that exponentially increases near the interface, but begins to decrease as the distance from the interface increases.

Chapter 2 gives the background for directional solidification, holography and interferometry. Chapter 3 describes the hardware apparati used in the project, while Chapter 4 gives the details for each experiment. Chapter 5 describes the steps needed to extract concentration profiles from an interferometric fringe pattern. The results are presented in Chapter 6 and conclusions are presented in Chapter 7, along with a discussion of various sources of error and suggestions for further work.

Chapter 2 Background

This chapter describes three basic topics that covered by this study. This includes the solidification process as it relates to this project, the theoretical basis for interferometry as an optical processor, and the history and theory for applied holography.

2.1 Solidification

This subsection covers a few of the various topics associated with solidification as they relate to this project. The types of directional casting available are discussed, as well as the different morphologies that are created during the casting process. Gravitational effects on the solidification process are presented and the type of alloy used to model alloy solidification is discussed.

2.1.1 Casting

Casting, or pouring molten metal into a prefabricated mold of a desired shape, is an easy and economical method for producing parts of a desired form. The molten metal, when allowed to cool as heat escapes from the sides of the mold, solidifies in the shape of the mold container. The success of this metal forming technique can be measured by its longevity; casting of simple copper parts predates 4000 BC (Kurz and Fisher, 1989).

In the casting process called directional solidification, the direction of heat transfer is controlled such that heat flows in one direction. This ensures that the molten material growth is unidirectional as well, since solidification occurs in the direction opposite to heat flow. In contrast, castings that are not thermally controlled have growth in multiple directions depending on the direction of heat flow within the container. Typically, as heat is allowed to escape through the sides of the container, the solid material starts at the sides of the container and grows towards the center. Ice forming in an ice cube tray is a good example.

Since growth occurs at the microstructure level, and microstructure strongly affects the alloy properties, the strength and temperature properties of a metal alloy can be greatly enhanced by controlling the growth process. It is desirable to cast parts using directional solidification when these properties need to be high in order to perform their task.

There are two types of directional heat transfer that are generally used: directional casting and Bridgman directional solidification. The first simply uses a chilled wall to encourage conductive heat transfer in one direction. The second involves moving a temperature field across metal material such that the metal is liquefied and a reasonably constant, non-transient temperature gradient is established. As heat is conducted through the material from the hot side of the zone to the cool side, unidirectional solidification is promoted.

Solidifying alloys undergo a complex growth process. First, the material loses specific heat as its temperature decreases, and latent heat as the material changes from liquid to solid. Second, since new solid material generally has a different concentration than the liquid in contact with it (one of the constituents is preferentially incorporated into the solid phase), solutal gradients are created during the solidification process. This mix of thermal and solutal changes creates a complicated solidification system with an associated complex density distribution. The growth process becomes strongly affected by the presence of gravitational forces.

2.1.2 Solidification Structures

Depending on the thermal and solutal profiles, and the rate at which they change within the solidification system, liquid alloy material will grow in one of three general growth morphologies: planar, cellular, and dendritic. The latter is usually characteristic of metal alloy solidification and is the growth morphology for the material used in this study. Dendrites are easily recognized by their secondary and higher order branches off of a primary trunk, as seen in Figure 1.

2.1.3 Gravitational Effects

During the solidification process, there is a large potential for buoyancy driven convection. This is especially true if the solidification process rejects solute that is less dense than the bulk solution. If the light liquid is located lower in a gravity field than the heavier bulk fluid, convection due to buoyancy is expected. Many researchers have spent considerable effort investigating the effect of gravity level on the solidification process (McCay et al, 1993; Johnston et al, 1983; Johnston et al, 1980; Iwasaki et al, 1992). These investigations include both experimentation under one gravity (1 g_e) and microgravity (10   g) conditions, as well as computer models bounded by both. Convection is important in the solidification process because it substantially mixes the

Figure 1 : Dendrites of an alloy model. In this image primary, secondary, and in some cases tertiary, arms are visible.

bulk liquid. This drastically changes the solutal profile from what would be expected in the absence of convection.

It has also been theorized, and there is substantial experimental observation, that buoyancy driven convection is strong enough to induce the breakage of secondary and higher order arms from the primary trunk (Sample and Hellawell, 1984; Copley et al, 1970). The flow may orient the broken piece of solid such that growth in a direction different from the original dendrite may occur. The resultant change in grain orientation produces an inhomogeneity in the solid microstructure that is detrimental to the cast part's strength properties (McCay et al, 1989; Christenson and Incropera, 1989; Chen and Chen, 1991).

Under microgravity conditions, there is virtually no buoyant potential, and therefore no convective flow is expected. However, due to solutal gradients created as a result of the growth process, there is diffusive mass transport taking place in the solution. In cases such as this, when diffusion is the primary mass transport mechanism, solidification of an alloy is termed diffusion limited growth. Without the strong convective flows observed while under the influence of gravity, dendritic growth in μg_e should have a more uniform growth pattern.

2.1.4 Metal Model Analogue

Aqueous ammonium chloride (NH_4Cl-H_2O) is important as a metal model for three reasons. First, the solution is transparent. This is desirable for using laser optical processing techniques like interferometry and confocal optical processors as optical measurement tools. Second, the solution solidifies at near room temperature (see phase diagram, Figure 2) so the material is much safer to work with and there are few of the problems associated with high temperature experiments. Also, very cold temperatures are not required to bring the solution to solid form. Last, but perhaps most important, the solution grows dendritically. In order to use ammonium chloride as a metal model analogue, it must have growth properties similar to actual metals. Virtually all metal alloys grow dendritically, and so any useful model of an alloy must grow likewise.

2.2 Interferometry

There are numerous types of optical processors available to measure properties of a transparent substance. An optical processor is a device that displays the way light is affected as it interacts with a material. In general, a beam of light that passes through a transparent medium will have the phase distribution of its field components modified. Optical processors visually display this modification. Interferometry, one type of processor, uses two separate coherent beams and the interference property of light to form visual fringes. The information they give are both qualitative and quantitative.

Two plane waves beams travelling in the x direction with arbitrary phases, ϕ_1 and ϕ_2, have electric field components given by

$$\bar{E}_1 = \bar{x}E_1\cos(\omega t - kz + \phi_1)$$
$$\bar{E}_2 = \bar{x}E_2\cos(\omega t - kz + \phi_2)$$

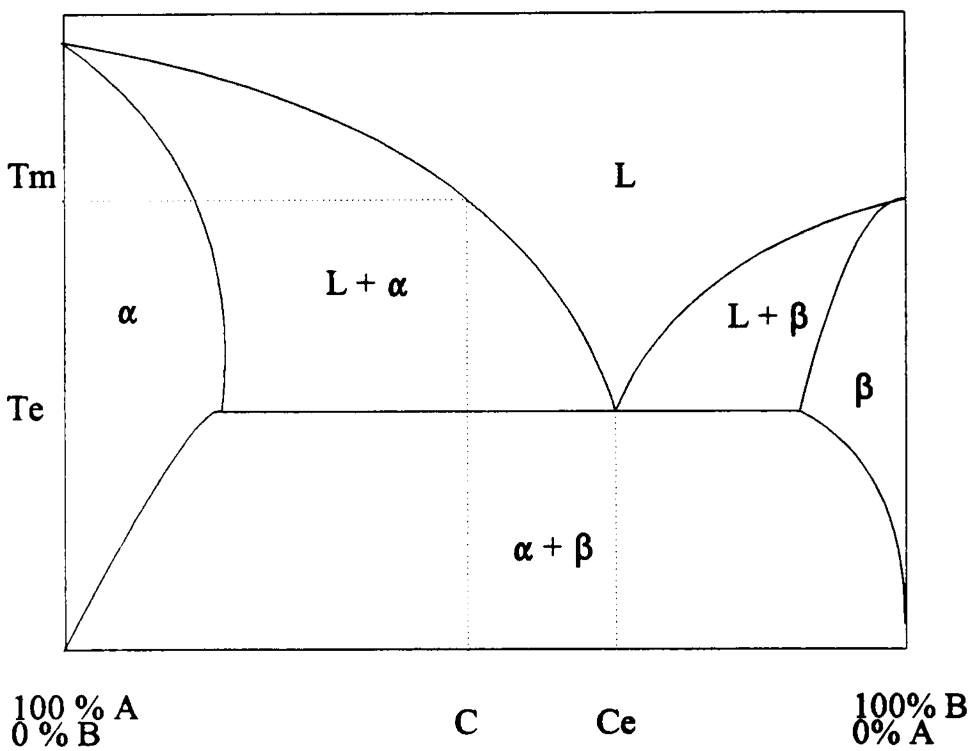

Figure 2 : A typical binary eutectic phase diagram. Tm is the melting temperature at a solution mixture of C. Te and Ce are the eutectic temperature and concentration respectively. For C = 28% NH_4Cl / 72% H_2O, Tm is about 24 °C.

where ω is the frequency of light and k is the wave number ($k = 2\pi/\lambda$). The total combined electric field is thus

$$\bar{E}_T = \bar{x}[E_1\cos(\omega t - kz + \phi_1) + E_2\cos(\omega t - kz + \phi_2)]$$

and its magnitude is

$$E_T = [E_1^2 + E_2^2 + 2E_1E_2\cos(\phi_1 - \phi_2)]^{1/2}$$

This electric field produces an intensity distribution

$$I = E_T^2 = E_1^2 + E_2^2 + 2E_1E_2\cos(\phi_1 - \phi_2),$$

which is essentially a base intensity ($E_1^2 + E_2^2$) modified by a sinusoid ($2E_1E_2 \cos(\phi_1 - \phi_2)$). The argument of cos is the difference in phase between the two incident electric fields. In the special case where $E_1 = E_2 = E$, this reduces to

$$I = a[1 + \cos(\phi_1 - \phi_2)]$$

which varies between 0 and 2a ($a = 2E^2$). This sinusoid intensity distribution, or fringe pattern, is thus related to the phases of the incident beams.

An optical tool that makes use of this principle can be constructed to measure this phase difference and direct measurement of these parameters can be made by relating phase to other parameters (density for example). In particular, a plane wave traveling through a transparent medium has its phase shifted in proportion to the refractive index of the medium. It is possible, therefore, to determine the index of refraction distribution by examining the fringe pattern of an interferometer, which depicts the phase differences in the two beams. Using known information about how a material's refractive index varies with temperature or concentration, for example, that parameter's distribution within the media can be determined. Optical setups of this sort are known as interferometers.

One particular interferometric setup is the Mach Zehnder Interferometer (MZI, Figure 3) (Mach, 1892; Zehnder, 1891). MZI uses two monochromatic coherent beams of light superimposed on an intensity detector. Typically the detector is a high resolution photographic emulsion or video camera array. In general, the superposition of two coherent beams produces an intensity distribution that contains regions of intensity both lesser and greater than the individual beams.

Usually, in a MZI configuration, the beam from a laser is divided using a beamsplitter, which assures coherence in the two beams. One of the beams passes through a transparent substance with an unknown index of refraction distribution, n(x,y,z). As the beam passes through the media (the beam is called the object beam) a phase change, $\phi(x,y)$, is introduced proportional to $\int n(x,y,z)\,dz$. The other beam (called the reference beam) propagates through the system without undergoing a significant phase change. Thus,

$$\bar{E}_o = \bar{x}E_o\cos(\omega t - kz + \phi(x,y))$$
$$\bar{E}_r = \bar{x}E_r\cos(\omega t - kz)$$

and the interferometric fringe pattern is given by

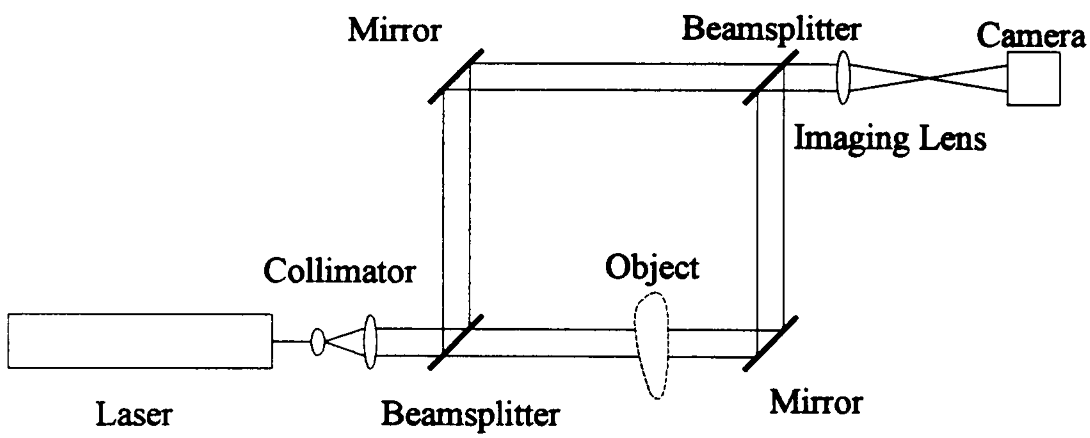

Figure 3 : Mach Zehnder interferometry. The object and reference beams are split from the same monochromatic source, and recombined on a light detector.

$$I = E_o^2 + E_r^2 + 2E_oE_r\cos(\phi(x,y)).$$

This is of the form

$$I = p[1 + q\cos(\phi(x,y))],$$

where

$$p = E_o^2 + E_r^2 \quad , \quad q = \frac{2E_oE_r}{E_o^2 + E_r^2}.$$

By measuring the spacing between fringes the phase change, $\phi(x,y)$, can be determined and a contour of phase values can be created. The phase contour can then be converted to an index of refraction distribution, which is used according to application needs.

2.3 Holography

2.3.1 Basic Principles

One particular field in optics that has seen tremendous advances with the advent of the laser is holography. Originally proposed by Gabor in 1949 as a procedure for achieving increased resolution in electron microscopy (Gabor, 1949; Gabor, 1951), holography is in many ways very similar to photography and they share a lot of the same principles.

To make a photographic print, there are two steps that must be performed. The first step involves illuminating the emulsion on a piece of film with an image, and developing the film so that the emulsion stops recording. The film from the first step is commonly called a "negative", because the recorded intensity distribution is the opposite of the incident intensity distribution. The second step requires re-illuminating the negative with light such that an intensity distribution is transmitted through the film. The transmitted distribution is again recorded on an emulsion and developed. This second "negative" is the opposite of the first, and hence the original light distribution is reproduced.

Holography is similarly a two step process. The first step is essentially the same as photography, in that an incident intensity distribution is recorded in an emulsion. However, rather than merely the object's image, the incident beam is the interference between the object beam, the beam emanating from the object, and a reference beam, similar to the reference beam used in interferometry. The beam incident on the emulsion is thus composed of many interference fringes. The second step in holography, however, is different from that of photography. The developed film is returned to its original position and re-illuminated with the reference beam. Instead of a single beam transmitted through the negative, a hologram (as the negative is called) produces three distinct beams. One beam is essentially the same as the original object beam incident on the film. The second beam is the conjugate of the first. The third beam is an amplitude modification of the incident reference beam used to reconstruct the hologram. The beams are called reconstructed object, conjugate, and transmitted beams respectively. The reconstructed object beam is interesting because it contains all the same phase information as the original incident object beam.

2.3.2 Holographic Recording

A typical optical setup for holographic recording is shown in Figure 4. Two coherent, monochromatic beams of the same wavelength are used. The first beam passes through (or reflects off) the object such that the phase of the beam is modified and falls onto the film. This beam is hereafter called the object beam. The second beam propagates through the optical system without introducing a phase shift. This beam is referred to as the reference beam. The object and reference beams are superimposed on high resolution film. Traditionally, the film emulsion is placed on a glass plate substrate, but an emulsion on a flexible acetate substrate may be used under circumstances where the weight and brittleness of glass is prohibitive.

The field components of the two electromagnetic waves incident on the film can be described as

$$\bar{\psi}_r = \psi_r \, e^{i[\omega t - kz - kx\sin\theta]}$$
$$\bar{\psi}_o = \psi_o \, e^{i[\omega t - kz + \phi(x,y)]}$$

where $\phi(x,y)$ is the phase shift introduced by the object and θ is the angle between the two waves. The combined electric field component on the film is

$$\bar{\psi}_{inc} = e^{i(\omega t - kz)} \, [\psi_o e^{i\phi(x,y)} + \psi_r e^{i(-kx\sin\theta)}]$$

and the recorded intensity distribution, I(x,y), is

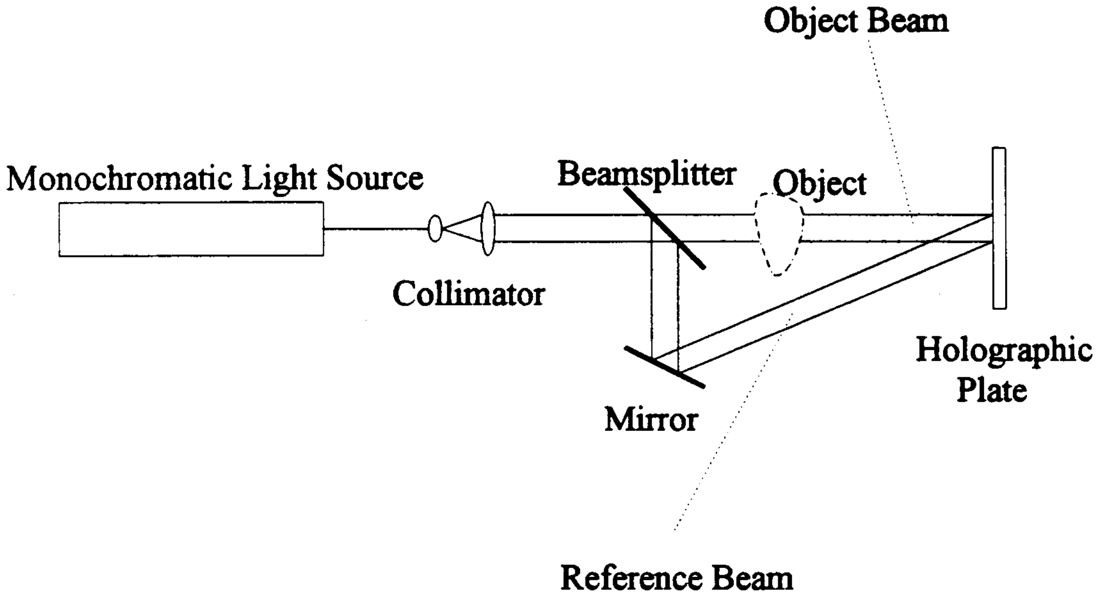

Figure 4 : A typical modern holographic recording setup. A single laser is used with a beamsplitter to produce separate reference and object beams.

$$
\begin{aligned}
I_{inc} &= |\bar{\Psi}_{inc}|^2 = |\bar{\Psi}_o + \bar{\Psi}_r|^2 \\
&= |\bar{\Psi}_o|^2 + |\bar{\Psi}_r|^2 + \bar{\Psi}_o\bar{\Psi}_r^* + \bar{\Psi}_o^*\bar{\Psi}_r \\
&= \psi_o^2+\psi_r^2 + \psi_o e^{i\phi(x,y)}\psi_r e^{-i(-kx\sin\theta)} + \psi_o e^{-i\phi(x,y)}\psi_r e^{i(-kx\sin\theta)} \\
&= \psi_o^2+\psi_r^2 + 2\psi_r\psi_o\cos[\phi(x,y) + kx\sin\theta],
\end{aligned}
$$

not unlike the fringe pattern produced by an interferometer. When the emulsion is developed, it has an amplitude transmittance described by

$$
t(x,y) \propto I_{inc} = \psi_o^2+\psi_r^2 + \psi_o e^{i\phi(x,y)}\psi_r e^{-i(-kx\sin\theta)} + \psi_o e^{-i\phi(x,y)}\psi_r e^{i(-kx\sin\theta)}
$$

2.3.3 Holographic Reconstruction

Traditional reconstruction of a developed hologram (Figure 5) requires re-illuminating the hologram with the original reference beam. In practice however, the high degree of coherence in lasers allows the use of a beam similar to the recording reference beam.

The electric field that is transmitted through the developed hologram,

$$
\begin{aligned}
\bar{\Psi}_{trans} &= t(x,y)\ \bar{\Psi}_r \\
&= t(x,y)\ \psi_r e^{i(\omega t - kz - kx\sin\theta)} \\
&= (\psi_o^2+\psi_r^2)\psi_r\ e^{i(\omega t - kz - kx\sin\theta)} \\
&+ \psi_o\psi_r^2 e^{i[\omega t - kz - \phi(x,y) - 2kx\sin\theta]} \\
&+ \psi_r^2\psi_o e^{i[\omega t - kz + \phi(x,y)]},
\end{aligned}
$$

has three terms. Each of these terms corresponds to a single beam emanating from the

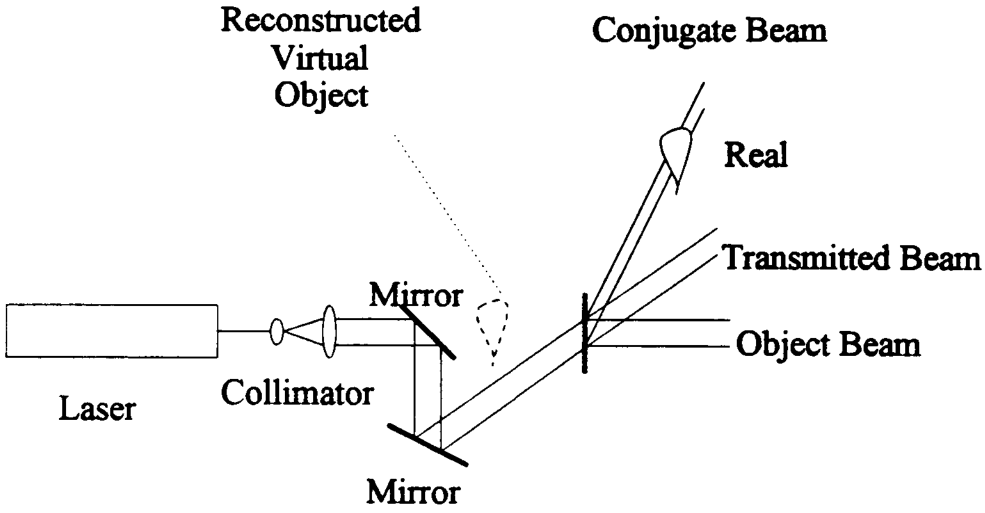

Figure 5 : A typical modern holographic reconstruction system. The virtual object and object beam are of interest.

hologram. The last term is an amplitude modification of the original object beam used to record the hologram. The "reconstructed" object beam (as it is called) contains all the phase information of the original object beam incident on the film during the first exposure.

2.3.4 Holography with Interferometry

Holography is ideally suited for incorporation into an interferometric setup. The object in an MZI is replaced with the reconstructed virtual object of a reconstructed hologram. By taking holograms of an object at various times, the phase characteristics of the object are recorded on film, and can be analyzed at a more convenient time later.

Chapter 3 Apparatus

This chapter describes the four major hardware apparati used in this project. These are the hardware necessary to: 1) directionally solidify an aqueous ammonium chloride, 2) record a hologram, 3) reproduce an image of the original object for analysis, and 4) acquire and analyze the reproduced image for quantitative value. All of these apparati except the second are located at the University of Tennessee Space Institute's Center for Laser Applications. The holographic recording is performed in NASA facilities at Marshall Space Flight Center (MSFC).

3.1 Solidification System

The solidification control system uses computer hardware and software to control the top and bottom surface temperatures of an optical quality quartz cuvette. The cuvette is filled with aqueous ammonium chloride of a desired concentration. Temperature control is maintained such that the solidification assembly models a Bridgman furnace.

3.1.1 Cuvette

Figure 6 illustrates the quartz cuvette in this project. The cuvette outside height, width, and depth dimensions are 29 mm x 20 mm x 12 mm and the inside dimensions are 25 mm x 16 mm x 8 mm respectively. The cuvette walls are each 2 mm thick. The fill tube attached to the cuvette serves as both a mechanism to add liquid to the cuvette and a region into which liquid can expand and contract. When filled with solution, the only

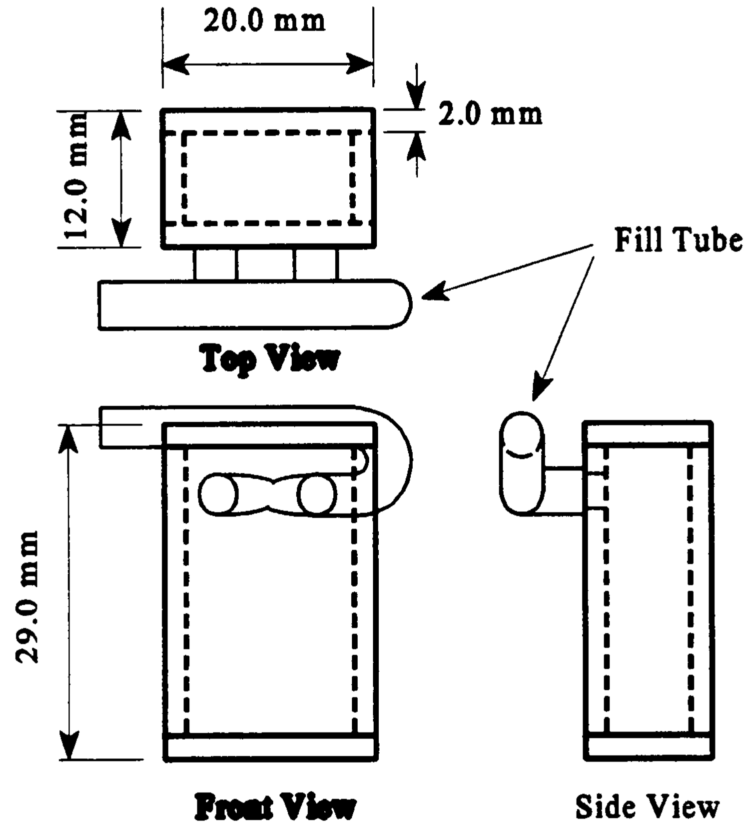

Figure 6 : Quartz cuvette used in the solidification system. The fill tube acts as a reservoir to allow for expansion and contraction of the liquid.

free gas/liquid interface is maintained in the tube. A plastic cap covers its end to prevent contaminates from getting into the cuvette.

3.1.2 Cuvette Assembly

A filled and capped cuvette fits into the assembly shown in Figure 7. High conductivity thermal grease is applied to the top and bottom surfaces of the cuvette to maintain good thermal contact with the assembly. Thermocouples are placed between the cuvette top and bottom surfaces and two, square, 25 mm x 25 mm copper plates. A slot cut into each of the plates is designed to contain a thermocouple. Thermal grease is placed between the copper plates and thermoelectric devices (TEDs), mechanisms that heat and cool based on the direction of electric current through them. The TEDs are mounted on copper blocks that serve as heat sinks. To extract excess heat, the blocks have tunnels drilled through them that allow water circulation. The blocks are stacked together using four angle brackets which hold the assembly together.

3.1.3 Solidification Control

Control of the solidification process is maintained using an IBM XT compatible personal computer fitted with a data acquisition device (Figure 8). The data acquisition device reads analog voltage signals from the thermocouples, converts the signals to digital and sends them to the PC, where they are converted to temperatures. Depending on what temperatures the surfaces of the cuvette should be, the computer decides what voltages should be sent to the TEDs to heat or cool the cuvette. The computer sends

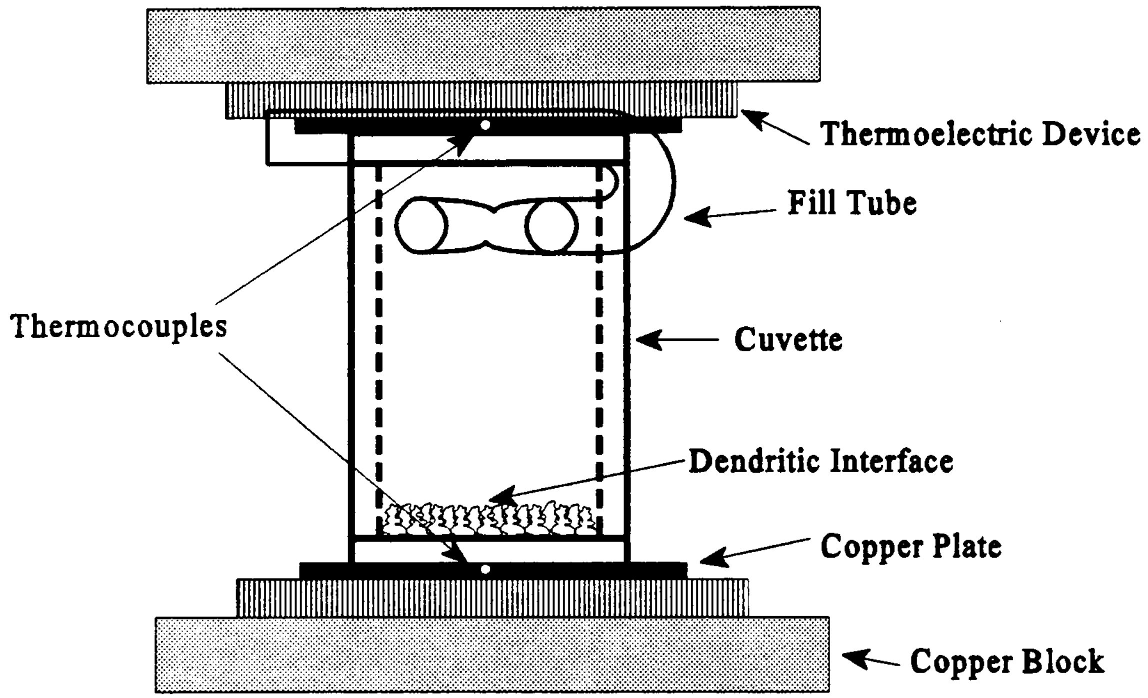

Figure 7 : Cuvette assembly for solidification system. The copper blocks are fitted with circulatory tubes so water can be remove excess heat generated by the thermoelectric devices.

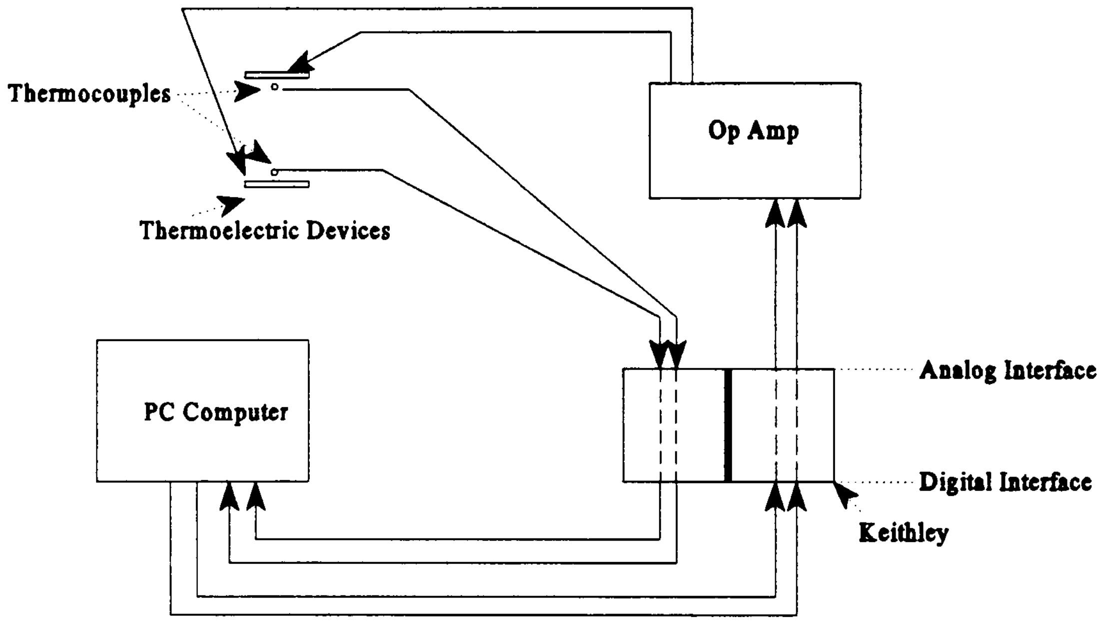

Figure 8 : Schematic of the solidifcation control system. The PC computer communicates digitally with the data acquisition device (Keithley). The data acquisition device reads and sends analog voltages from the thermocouples and op amp respectively.

digital signals representing these voltages to the data acquisition device, where the digital signals are converted to analog voltages. An operational amplifier scales the voltages to values that drive the TEDs, heating or cooling the cuvette surface.

3.2 Holographic Recording

NASA has two holographic setups for recording holograms. The Fluids Experiment System (FES) is a flight ready optical system that can be installed on the space shuttle for holographically recording fluid experiments under microgravity (μg_e) conditions. NASA Marshall's Holographic Ground System (HGS) is a facility for both recording holograms under 1 earth gravity (1 g_e) conditions and reconstructing recorded holograms.

3.2.1 FES

To record holograms under μg_e conditions, NASA has the FES (Figure 9), an optical setup to take holograms of specific fluid experiments on board spacelab. FES has flown twice; once aboard Spacelab-3 in 1985 and once aboard IML-1 in 1992. Its design allows for simultaneous holographic recordings along a primary and secondary axis. The optical setup consists of a helium neon (HeNe) laser operating at 632.8 nm, collimated using a parabolic mirror and lens. The beam passes through a beamsplitter, separating the single beam into two separate ones. One of the beams is the reference beam for the primary axis hologram. The second beam is split again, one of these becoming the reference beam for the secondary axis hologram while the other beam is directed through

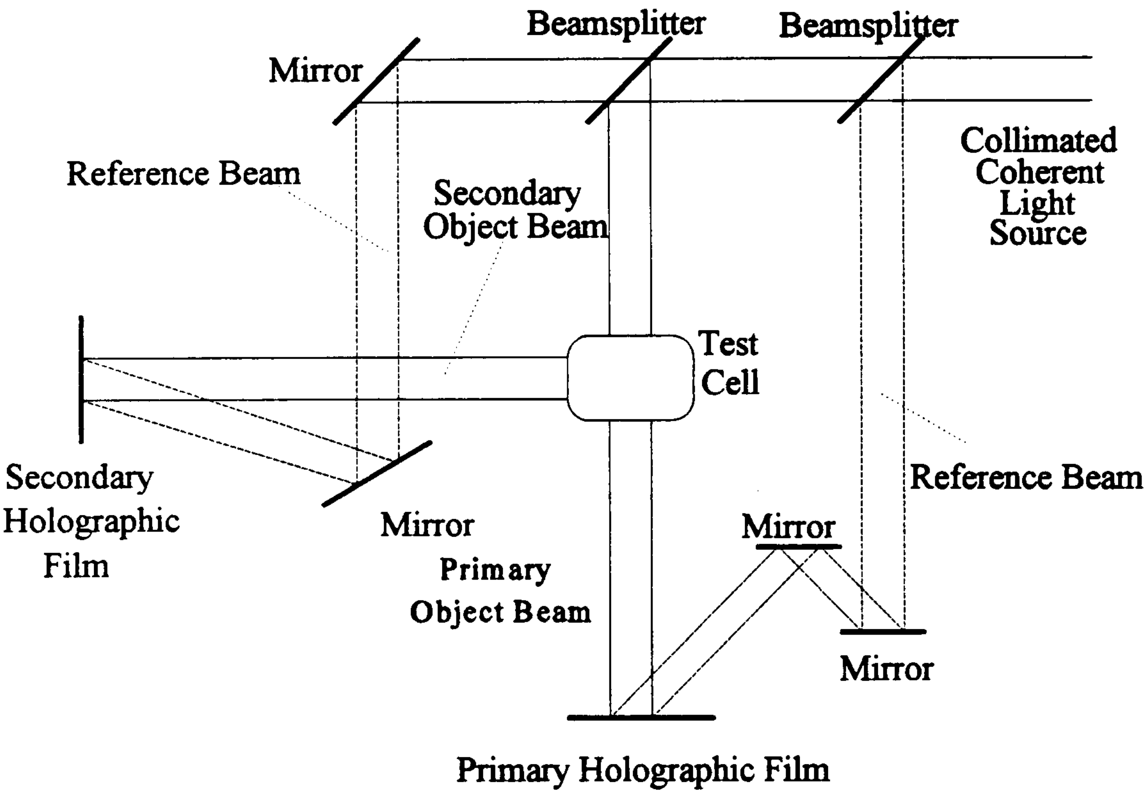

Figure 9 : Schematic of the optical setup for the Fluids Experiment System (FES). FES allows for two views of the object to be recorded simultaneously.

the test cell. The beam that passes through the test cell, now referred to as the primary object beam, recombines with the primary reference beam on holographic film to form the primary hologram. Scattering from the primary object beam in the test cell creates the secondary object beam, which recombines with the secondary reference beam on holographic film to produce the secondary hologram. Hologram development procedures for holograms recorded in FES are discussed in Chapter 4.

3.2.2 HGS

To provide the capability to record holograms during ground-based experiments, NASA constructed the Holographic Ground System (HGS), shown in Figure 10. HGS also uses a HeNe laser operating at a wavelength of 632.8 nm. The beam is collimated and split into the corresponding object and reference beams. The object beam passes through the test cell and recombines with the reference beam on the holographic film. Hologram development procedures for holograms recorded in HGS are discussed in Chapter 4.

3.3 Holographic Reconstruction

Developed holograms were reconstructed in the University of Tennessee Space Institute's Solidification Physics Laboratory. The reconstructed object beam was combined with a reference beam to form a MZI setup, so that quantitative analysis could be made (Figure 11). Appendix A1 lists the individual parts for the equipment used for holographic reconstruction and interferometry. A 60mW helium neon laser is used as a

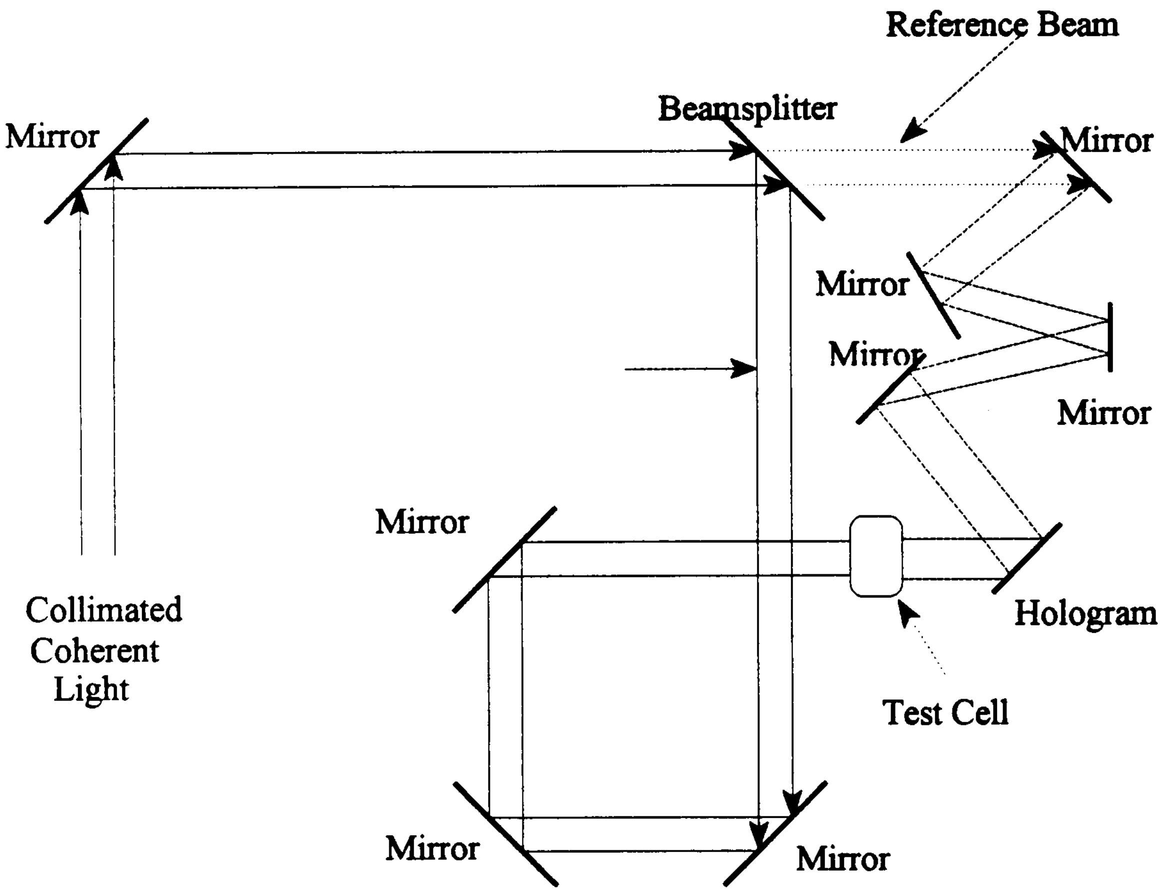

Figure 10 : The optical setup for recording holograms at the Holographic Ground System (HGS).

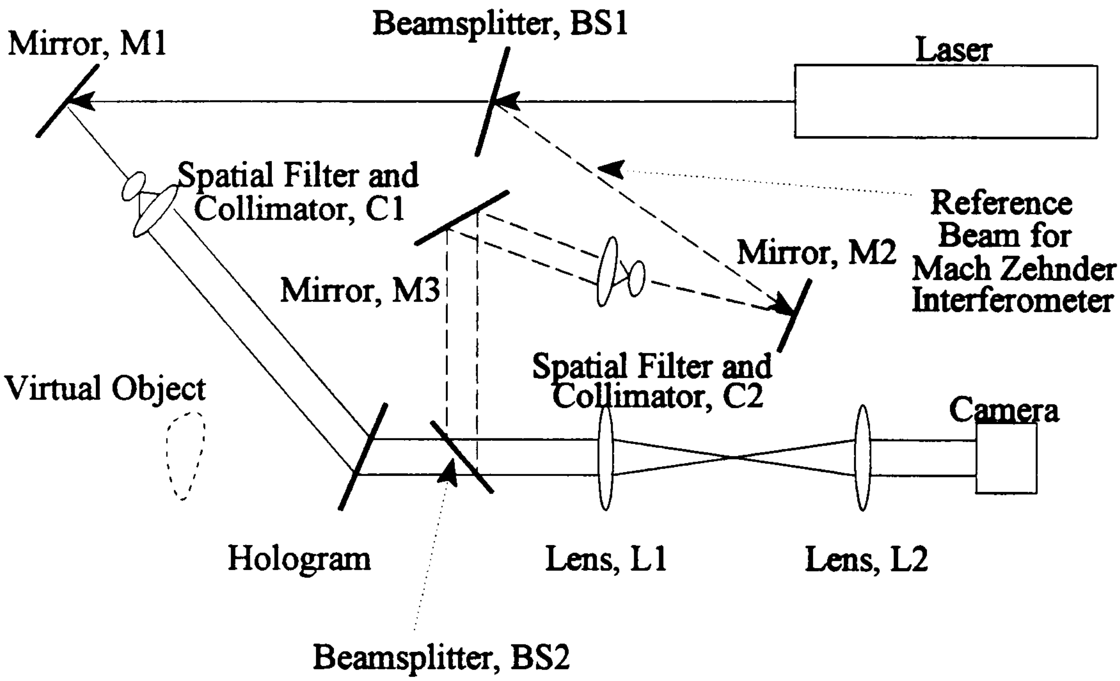

Figure 11 : UTSI's holographic reconstruction system with Mach Zehnder interferometry.

coherent, monochromatic light source. The laser's raw beam is split on a variable ratio beamsplitter. One beam is directed through a spatial filter (10μm pin hole) and 50 mm collimator using a plane mirror. The collimated beam strikes the hologram, vacuum mounted on a glass holder, and produces the reconstructed object beam. The other beam is directed through a spatial filter (4.6 μm pinhole) and 50 mm collimator. This beam recombines with the reconstructed object beam near the hologram in a cube beamsplitter. The combined interfering beams are sent through a two lens confocal optical imaging system onto the imaging array of a video camera, used to display the interference pattern on a video monitor.

3.4 Image Acquisition

Image acquisition makes use of video recorded on standard VHS format video tape. By recording on video tape, the reconstructed image can be stored for long periods of time, and the image may be easily recalled without having to reconstruct the hologram additional times.

Data Translation image processing hardware and software are used to digitize video images from VHS format tapes. The hardware and software provides the capability to store digitized images on magnetic media and to digitally enhance images, making desired features more visible.

Appendix A2 is a list of the various components in the image processing computer system. The software on the computer uses FORTRAN callable functions provided by Data Translation, and gives the ability to digitize images from an input video signal, store and recall the images to disk, and make limited image enhancements (such as changing image contrast or performing histogram equalization). Digitized and recorded images are used for data reduction.

Chapter 4 Experimental procedure

Three sets of experiments were performed in this study and each set uses a different solution concentration. The first set uses pure de-ionized H_2O. The second set uses aqueous ammonium chloride with a mass ratio of 72/28 water/NH_4Cl. A solution of this composition will be referred to as NH_4Cl 72 wt% H_2O. Similarly, the third set uses an aqueous ammonium chloride solution with a mass ratio of 71.5/28.5 H_2O/NH_4Cl and is referred to as NH_4Cl 71.5 wt% H_2O.

An "experiment" in this project is defined as follows: starting with a solution of a given concentration in a quartz cuvette, the top and bottom surface temperatures are set to a certain value, establishing a temperature gradient across the cuvette. After the temperature and solutal fields in the cuvette reach near steady-state (this time period is referred to as the gradient hold), the top and bottom surface temperatures are lowered at a given rate (referred to as the temperature ramp). At selected times in the experiment, a hologram is taken. For the first set of experiments, holograms were taken during the gradient hold and temperature ramp. During the solidification experiments, holograms were taken only during the temperature ramp.

This chapter describes in detail the steps taken for each experiment. These steps include making solution, filling a quartz cuvette with solution, placing the cuvette in the cuvette assembly, placing the assembly into a holographic recording setup, recording holograms, and analyzing each hologram for data. The hardware used in each of these stages was described in Chapter 3.

4.1 Solution Preparation

Three different concentrations of aqueous ammonium chloride were used. For the first set of experiments, hereafter called the GSRP water runs, the solution consisted of 100% H_2O, and was used to optically measure the temperature gradient in a liquid under an approximately linear temperature distribution. The second and third solutions, comprised of NH_4Cl 72 wt% H_2O and NH_4Cl 71.5 wt% H_2O, respectively, solidify dendritically when the temperature of the liquid is near room temperature (24 °C). Hereafter, the experiments that use the 72 wt% H_2O solution are referred to as the GSRP 1 g_e solidification runs and the experiments that use the 71.5 wt% H_2O solution are referred to as the CAST 1 μg_e solidification runs.

A small flexible 6" plastic hose attached to a syringe and needle was used to fill a quartz cuvette. For the GSRP water run experiments, the syringe was slowly filled with pure water and injected into the cuvette such that all air, including small bubbles, was removed from the cuvette, and the only free liquid/gas surface contained within the fill tube.

In the GSRP 1 g_e solidification runs, 72 wt% H_2O solution was created by carefully adding 2.57 grams of H_2O for every 1.00 gram of NH_4Cl to an airtight plastic container. The constituents' masses were measured on a digital scale. With both components in the plastic container and the container's lid secured tightly, vigorous shaking mixed the solution until the NH_4Cl was completely dissolved. Generally, about 150 grams of solution was created at one time.

Before filling the cuvette with solution, the liquid temperature is raised to about 50 °C by placing the plastic container with solution in a water filled beaker, heated on an electric plate. This melted any solid material that may have been present in the container to insure a uniform initial concentration. The same procedure was used to fill the cuvette as was used for the GSRP water runs. Unused solution was kept stored in the plastic container.

The CAST μg_e solidification runs used a solution consisting of NH_4Cl 71.5 wt% H_2O. Making the solution and filling the cuvette were essentially the same as for the second solution type, except that 2.51 grams of H_2O was added to every 1.00 gram of NH_4Cl.

4.2 Growth Conditions

Since this project investigates the thermal and solutal profiles of a dendritic interface and is not investigating the process of nucleation, it was desirable to have a small amount of solid present in the cuvette at the start the growth process for the GSRP 1 g_e solidification runs and CAST μg_e solidification runs. For the GSRP solidification runs, the solution was nucleated before the experiment began by chilling the cuvette top and bottom surfaces well below the solutions's liquidus temperature (around 24 °C) if solid material was not already present. The TEDs were used to lower the cuvette surface temperatures to about 0 °C, and the solution nucleated after a short period of time. For the CAST μg_e solidification runs, astronauts verified the presence of solid material within the cuvette before each experiment began. At the start of each solidification experiment, there was a small amount of solid ammonium chloride present in the cuvette.

For the GSRP water and 1 g_e solidification runs, the cuvette was inserted into the cuvette assembly shown in Figure 7 of Chapter 3. Once the assembly had been determined to function properly, the assembly was inserted into the holographic recording system at HGS. For the CAST μg_e solidification runs, the quartz cuvette was sealed in a CAST Science Module (CSM), an optical box functionally equivalent to the cuvette assembly, for use on the space shuttle. Additionally, the CSM was put into the CAST Optical Bench Adaptor (COBA), a device for fitting the CSM into FES. Table 1 gives the different cooling rates and temperatures associated with each experiment.

The top and bottom temperatures of the cuvette were set by computer to the values indicated by T_{top} and T_{bot} in Table 1 and allowed to remain in the gradient hold for the periods of time given. After the gradient hold, the top and bottom temperatures were lowered at the specified cooling rates for a desired period of time, and the experiment ended. A typical temperature profile for the cuvette top and bottom temperatures is shown in Figure 12.

4.3 Holographic Recording

The holographic recording medium is 70 mm Kodak SO-253 Holographic Film for the μg_e runs and Agfa-Gevaert 10E75 Holotest 4" x 5" glass plates for the GSRP experiments. Average exposure time was about 60 ms, depending on the intensity level

Table 1 : Parameters associated with each experiment.

	Experiment	Initial Temps T_{top}/T_{bot} (°C)	Gradient Hold (minutes)	Cooling Rate (°C/hr)
GSRP Water Runs	Run GW1	80/20	125	60
	Run GW3	80/10	100	60
GSRP 1 g_e Solidification Runs	Run GS4	55/17	138	60
	Run GS5	53/15	90*	18
	Run GS6	53/15	68	120
	Run GS8	53/15	122	180
CAST μg_e Solidification Runs	Run CS7	67/22	60	13.5
	Run CS8	67/22	24	67.5

* Estimated

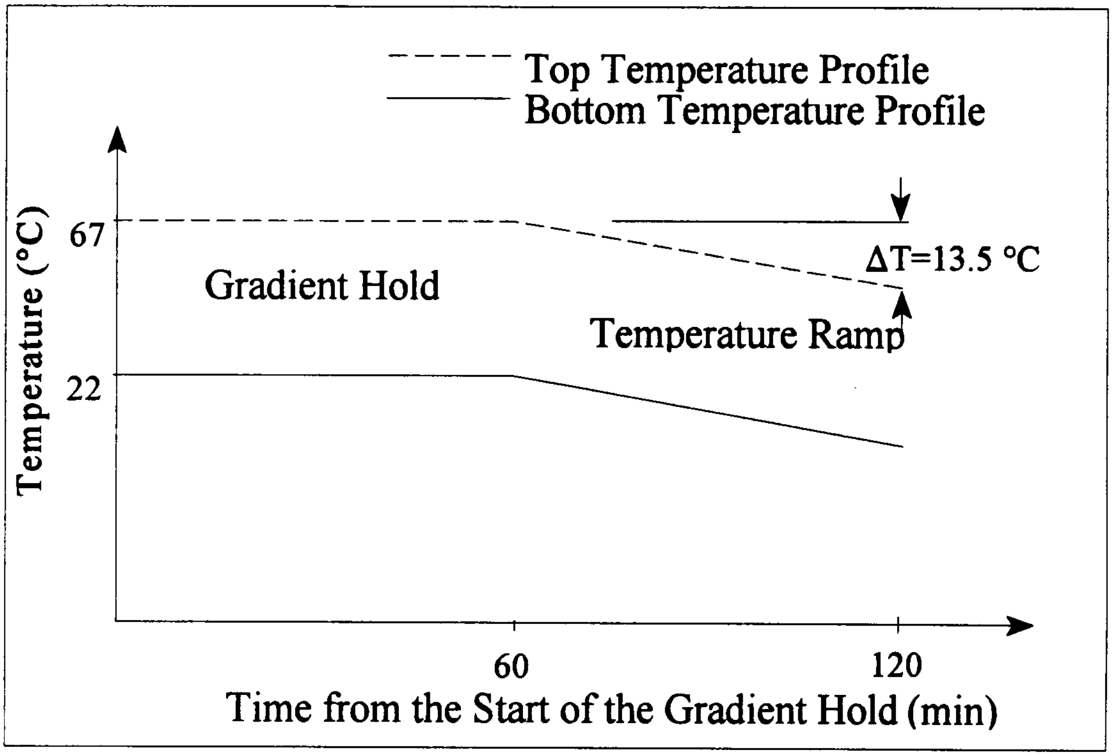

Figure 12 : A typical temperature profile for each of the experiments (CAST μg_e solidification Run CS7 shown). The gradient hold period of time is used to bring the temperature and solute fields within the cuvette to equilibrium. The temperature ramp brings the temperatures down at a desired rate.

incident on the film. Holograms were taken at desired intervals during the gradient hold and ramp, as shown in Table 2.

Convection substantially mixes the liquid fluid ahead of the interface, and while this significantly affects the growth process, it makes determining the thermal and solutal fields very difficult. The method of data reduction (Chapter 5) used to find these fields is designed to yield concentration and temperature gradient data for a liquid limited to diffusive heat and mass transfer. Therefore, holograms were taken before the onset of buoyancy driven convection.

The desired frequency and recording times for taking holograms depended on the experiment. The GSRP water runs are inherently stable with respect to buoyancy driven convection. As the bottom of the cuvette was cooler than the top, the liquid increases in density with height. There is no potential for buoyancy driven convection and so holograms could be recorded at any time during the experiment. However, with the solidification runs, the solidification process generates a solutal field which, coupled with the temperature distribution, creates the potential for buoyancy driven convection. Therefore, holograms had to be taken before this breakdown occurred.

The approximate times when convective breakdown occurs under the influence of 1 g_e have been determined (Hopkins, 1989; McCay et al, 1989), and this set of data was used to determine the recording times for the GSRP 1 g_e solidification runs. For this set of experiments, the recording medium (glass plate) had to be inserted manually into the holographic recording setup. Since convective breakdown occurs just minutes after the start of the temperature ramp, only one hologram could be taken for each of the GSRP

Table 2 : Quantity of holograms and recording times for each of the eight experiments.

	Experiment	Number of holos/exper	Time from start of Gradient hold (min)	Time from start of Ramp (min)
GSRP Water Runs	Run GW1	2	85.0, 92.0	
	Run GW3	2	89.5	9.7
GSRP 1 g_e Solidification Runs	Run GS4	1		1.5
	Run GS5	1		3.0
	Run GS6	1		1.0
	Run GS8	1		0.75
CAST μg_e Solidification Runs	Run CS7	2		55.6, 60.63
	Run CS8	2		12.12, 16.15

solidification runs during the temperature ramp before convective breakdown occurred. None of the holograms taken in this set were recorded during the gradient hold.

Under microgravity conditions, as was the case with the CAST μg solidification runs, the potential for buoyancy driven flow is minimized, and holograms could be taken at much later times in the temperature ramp period.

4.4 Holographic Reconstruction

Holograms were developed according to the procedures given in Tables 3 and 4 and inserted into the reconstruction system described in Chapter 3. For the CAST μg solidification runs, the Kodak film holograms were vacuum mounted on a high quality glass window. For the GSRP runs, a Newport Model 520 Plate Holder was used. For either piece of equipment, the hologram was oriented such that the reconstructed object beam is transmitted down the length of the optical table, an orientation convenient for viewing.

Once the hologram was in place, a two lens imaging system and camera produced images of the reconstructed object. The position of the lenses, their focal lengths, and the position of the camera all determine the magnification of the focused image. Simple thin lens theory predicted the general position of each of the components. Once these locations were determined and the components were in place, small changes were made to provide a clear, in-focus image.

Table 3 : Development procedure for Agfa-Gevaert Holotest plates

Step	Action	Solution	Time
1	Develop	Kodak D-76	6.5 minutes
2	Rinse	Kodak Stop Bath	30 seconds
3	Fix	Kodak Fixer F-5	5-10 minutes
4	Rinse	Running water	20-30 minutes
5	Rinse	Kodak Photo-Flo	5 seconds

Table 4 : Development procedure for Kodak SO-253 70 mm holographic film.

Step	Action	Solution	Time
1	Develop	Kodak D-19	6 minutes
2	Rinse	Kodak Stop Bath	10-30 seconds
3	Fix	Kodak Fixer F-5	5-10 minutes
4	Wash	water	1 minute
5	Rinse	Kodak Hypo Cleaning	4 minutes
6	Wash	water	3 minutes
7	Rinse	75/25 Methanol/water	5 minutes
8	Wash	water	5 minutes
9	Rinse	Kodak Photo Flo	5 seconds

4.5 Interferometry

With the object beam ready and the reconstructed object in focus, the reference beam of a MZI setup was added to the optical system. By removing an opaque stop from the path of the reference beam between the two beamsplitters, the reference beam could be aligned with the object beam using mirror M3 and beamsplitter BS2 (Figure 11, Chapter 3). Once aligned, the reference beam was displaced from this position by introducing a small angle about the objects horizontal axis using M3 to add the carrier frequency fringe pattern needed by the Fourier transform method (Chapter 5)..

4.6 Image Recording

A standard monitor/VCR combination enabled the resulting fringe pattern to be viewed and recorded on standard VHS format videotape. Two fringe patterns were needed (by the Fourier transform method) to find each solutal profile. The first view is of an area outside the cuvette where there is no significant difference in the optical paths of the object and reference beams. The fringe pattern is due solely to the angular difference between the two beams of the MZI. The second view is the region of interest within the cuvette. The fringe pattern there is due to the combined effects of the reference tilt and differences in the index of refraction of the transparent fluid. For each hologram, an image of the region outside the cuvette was recorded, along with different regions of interest within the cuvette. For the GSRP holograms, two different regions within the cuvette were recorded. For the CAST holograms, three regions within the cuvette were recorded. Each image occupies approximately 10 seconds of video tape time.

Chapter 5 Data Reduction

There are several methods for creating interference fringes including the one used in this project, Mach Zehnder interferometry. However, while interference fringes visually give qualitative information about these processes, achieving quantitative results requires a scheme for extracting information. This chapter details the steps necessary to reduce quantitative data from an interferometric fringe pattern.

The phase distribution is calculated using two different methods: Fourier transform and intensity. The phase distribution is converted to an index of refraction distribution by relating $\phi(x)$ to $n(x)$. Finally, using an experimentally determined relationship for index of refraction as a function of temperature and concentration, the concentration distribution is calculated.

5.1 Converting Fringe Patterns to Phase

Two different methods of determining phase are examined. The first method, Fourier transform, is well suited for automated analysis, although the analysis itself is complicated. The second method, "intensity", is very simple to apply, but does not lend itself to an automated process.

5.1.1 Fourier Transform

The Fourier transform method uses Fourier domain processing to isolate the phase distribution in an interferometric fringe pattern. The procedure described here was developed by Magnani (Magnani, 1992) and uses two independent images. The first image contains fringes due to a phase change between the reference and object beams of the interferometer and the angle between the two beams, while the second contains fringes due to the angle only. The former is hereafter referred to as the experimental or fringe image, while the latter image will be referred to as the carrier image.

The experimental and carrier images can be mathematically described as

$$I(x,y) = a(x,y) + b(x,y)\cos(2\pi f_0 x + \phi(x,y))$$
$$I_c(x,y) = a_c(x,y) + b_c(x,y)\cos(2\pi f_0 x + \phi_0)$$

respectively. $\phi(x,y)$ is the desired phase shift due to the thermal and solutal profiles within the cuvette.

The carrier intensity distribution may be made one dimensional by examining the intensity distribution along constant y such that:

$$I_c(x) = a_c(x) + b_c(x)\cos(2\pi f_0 x + \phi_0)$$

By taking the Fourier transform of $I_c(x)$

$$\mathcal{F}[I_c] = \mathbf{I}_c(f) = \int_{-\infty}^{\infty} I_c(x) e^{i2\pi f x} dx$$

the function converts into the frequency spectra. $\mathbf{I}_c(f)$ has the form of three peaks; one at $f = 0$, one at $f = f_0$ and one at $f = -f_0$. By filtering the Fourier domain curve and isolating one of the off axis peaks, f_0 can be determined.

Similarly, the experimental image can be made one-dimensional by examining the intensity distribution along constant y to yield

$$I(x) = a(x) + b(x)\cos(2\pi f_0 x + \phi(x)).$$

Introducing a new variable, c(x),

$$c(x) = \frac{1}{2}b(x)e^{i\phi(x)}$$

and making use of Euler's transformation, I(x) can be rewritten as:

$$I(x) = a(x) + c(x)e^{i2\pi f_0 x} + c^*(x)e^{-i2\pi f_0 x}$$

where c* is the complex conjugate of c.

The Fourier transform of I(x) yields

$$\begin{aligned}\mathcal{F}[I] = \mathbb{I}(f) &= \int_{-\infty}^{\infty} I(x)e^{i2\pi fx}dx \\ &= \int_{-\infty}^{\infty}[a(x) + c(x)e^{i2\pi f_0 x} + c^*(x)e^{-i2\pi f_0 x}]e^{i2\pi fx}dx \\ &= A(f) + C(f+f_0) + C^*(f_0-f)\end{aligned}$$

where

$$\begin{aligned}A(f) &= \mathcal{F}[a(x)] \\ C(f) &= \mathcal{F}[c(x)]\end{aligned}$$

This function, in the frequency domain, also has the form of three peaks; one centered around f = 0, one near $f = f_0$, and one near $f = -f_0$. Bandpass filtering can be used to isolate one of the off axis peaks, and shift the spectra is to the origin using f_0 to obtain

C(f). From this, applying the inverse Fourier transform will yield the original function c(x):

$$c(x) = \int_{-\infty}^{\infty} C(f) e^{-i2\pi f x} df$$

which in turn yields the phase change, $\Delta\phi(x) = \phi(x) - \phi_0$, obtained by taking the imaginary component of the complex log of c(x):

$$\Delta\phi(x) = Im[\ln\ c(x)].$$

In performing these steps, the background intensity, a(x), and fringe intensity variations, b(x), have been removed.

5.1.2 Intensity

An alternative to the Fourier transform method for determining $\Delta\phi(x)$ is to make the reference and object beams in the interferometer parallel, thus removing the carrier frequency, f_0, from the fringe pattern. In this manner, the fringes visible in the intensity distribution are a result of temperature and concentration only. The intensity distribution can be written mathematically as

$$I(x) = a(x) + b(x)\cos(\phi(x)).$$

From this, it is apparent that the phase change between consecutive fringe extrema is 2π. A phase distribution can be created by manually examining the position of each fringe extrema and assigning an incremental phase value to that position.

extrema and assigning an incremental phase value to that position.

5.2 Converting Phase to Refractive Index

Generally, $\phi(x)$ is the desired goal of fringe pattern data reduction. Depending on the needs of the researcher, other parameters may be determined from the phase. For this project the index of refraction, n(x), is one such goal because it can be related to concentration and thermal profiles within the cuvette. The change in n(x) may be calculated using the proportionality between phase and index of refraction (Born and Wolf, 1980):

$$\Delta n(x) = \frac{\phi(x)}{2\pi} \frac{\lambda}{d}$$

where λ is the wavelength of light and d is the integration length through the cuvette. When the intensity method is used to produce $\phi(x)$, this can be simplified to

$$\Delta n(x) = \frac{(2\pi/fringe)}{2\pi} \frac{\lambda}{d} = \frac{7.91 * 10^{-5}}{fringe}.$$

Thus there is a $7.91 * 10^{-5}$ change in n(x) between consecutive fringes in a fringe pattern without a carrier frequency.

5.3 Converting Refractive Index to Concentration

For each of the experiments (GSRP water, GSRP 1 g_e solidification, and CAST μg_e solidification), the 1 dimensional liquid index of refraction is calculated using the

$$n(C,T) = 1.3674 - 1.1180 * 10^{-4}\,(T - 25°C) + 1.8861 * 10^{-3}\,(C - 19\ wt\%\ NH_4Cl\text{-}H_2O),$$

an equation developed at UTSI (McCay et al 1994) to show the dependence of index of refraction on temperature and concentration.

What is important to note is that converting phase to refractive index only determines the shape of the refractive index curve, $\Delta n(x)$. In order to determine n(x) itself, a boundary condition is required. For purposes of measuring concentration, however, $\Delta n(x)$ is sufficient to calculate $\Delta C(x)$, the change in concentration in the region over which $\Delta n(x)$ is measured. Similarly, a concentration boundary condition is required to produce C(x) directly. The concentration in the liquid approaches the bulk concentration (C_o) as x approaches ∞ (or a sufficiently large value). For the experiments studied, the concentration in the liquid usually approaches C_o within a distance of 4 mm above the interface (depending on the growth conditions).

Chapter 6 Results

This chapter gives the results of applying the data reduction schemes described in Chapter 5 to the fringe patterns created by the procedures discussed in Chapter 4. Using the Fourier transform method, index of refraction profiles are given for all three experimental sets, and concentration profiles are given for the solidification runs. The intensity method of reducing data is compared with the Fourier transform method.

6.1 Experimental Results

6.1.1 GSRP Water Runs

Figure 13 is a composite of the three images used to determine the index of refraction of water using the Fourier transform method for one of the GSRP water run holograms (Run GW1). The first image (on the left) of the composite is a section of the carrier frequency image (CARRIER.IMG). The second image (in the center) contains the experimental fringe pattern (FRINGE.IMG). The last image in the composite (on the right) is a section of the object image that generally displays features within the cuvette that are not visible in the experimental image as a result of the fringes. Raw data from the Fourier transform analysis method is given in Appendix B1.

The change in index of refraction in water over a four mm distance above the bottom of cuvette and 2.5 mm from the cuvette side wall is given in Figures 14,15, 16, and 17. Each figure contains two index of refraction profiles, corresponding to the left and right sides of the cuvette.

The index of refraction profiles show a nearly linear decrease in the index of

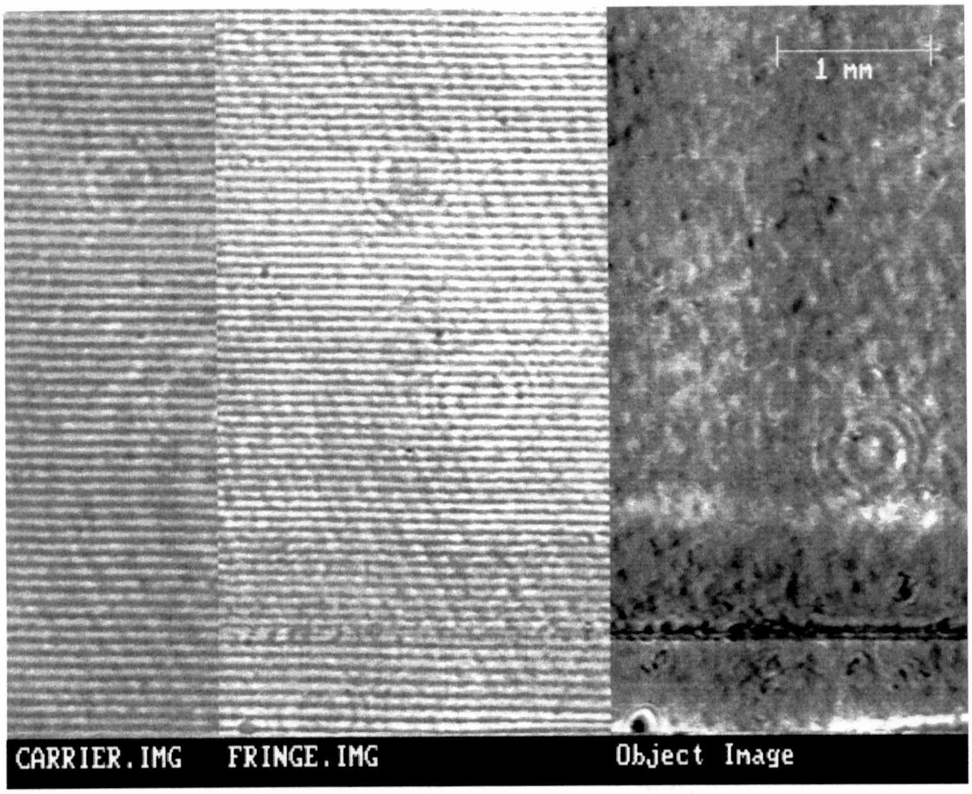

Figure 13 : Composite image of GSRP water Run GW1, hologram 1.

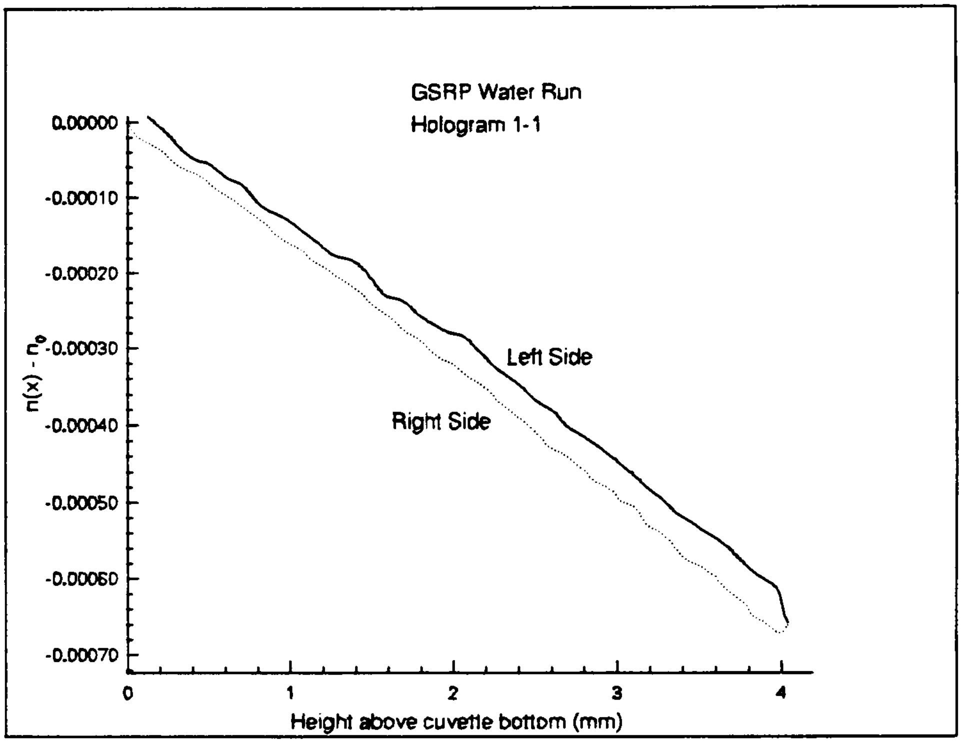

Figure 14 : Index of refraction profiles for GSRP water Run GW1, hologram 1 (85 minutes into the gradient hold). Each profile is taken approximately 2.5 mm from the sides of the cuvette.

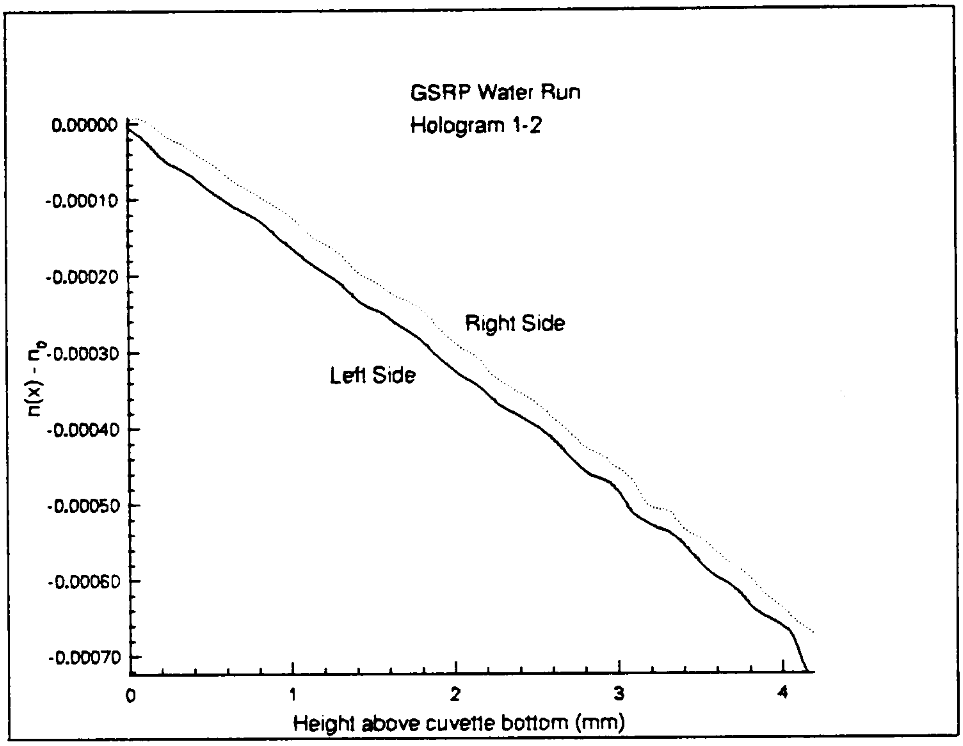

Figure 15 : Index of refraction profiles for GSRP water Run GW1, hologram 2 (92 minutes into the gradient hold). Each profile is taken approximately 2.5 mm from the sides of the cuvette.

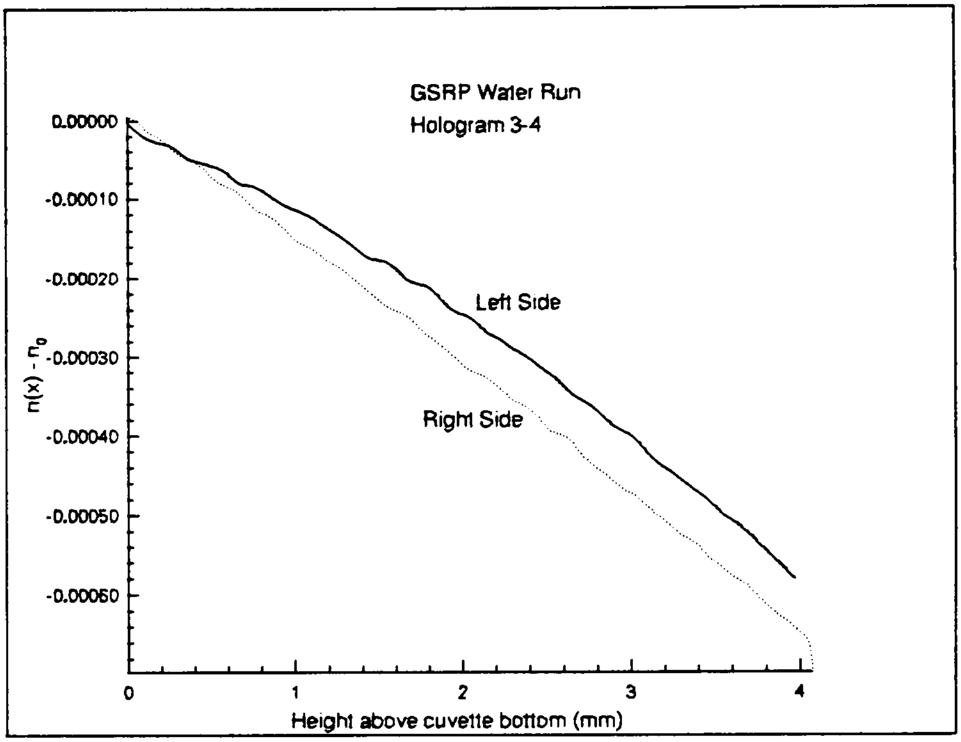

Figure 16 : Index of refraction profiles for GSRP water Run GW3, hologram 4 (89.5 minutes into gradient hold). Each profile is taken approximately 2.5 mm from the sides of the cuvette.

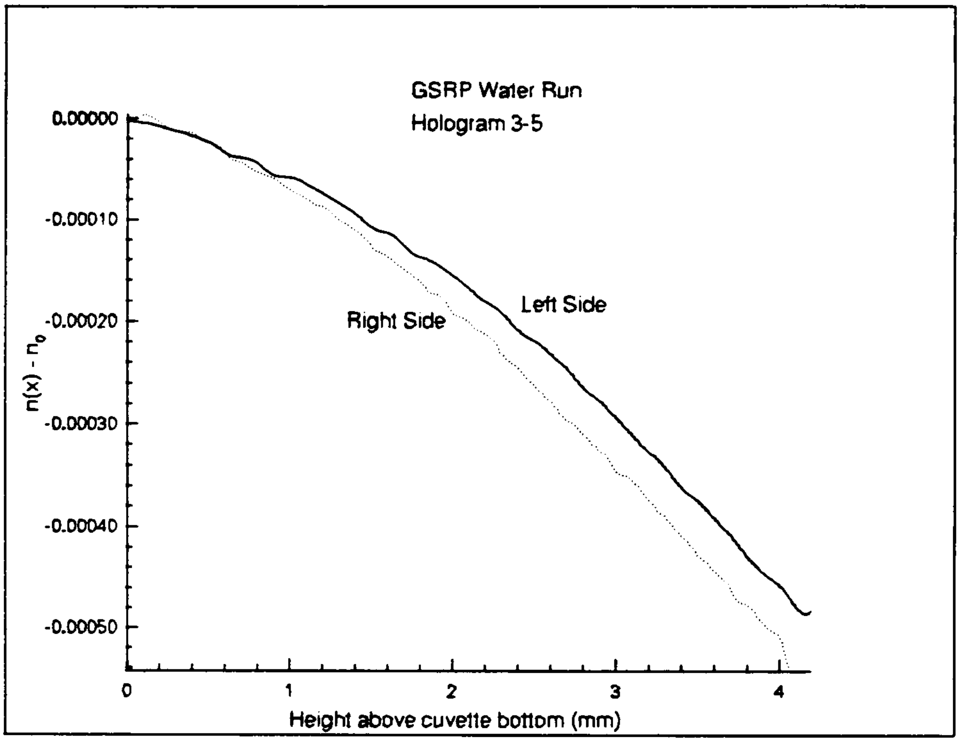

Figure 17 : Index of refraction profiles for GSRP water Run GW3, hologram 5 (9.7 minutes into temperature ramp). Each profile is taken approximately 2.5 mm from the sides of the cuvette.

refraction of water with height. For a positive temperature gradient (temperature increasing with height), this decrease in n is as expected. The similarity in shape of the curves indicates the degree of uniformity of temperature in the cuvette. For example, the nearly identical slopes of the two curves in Figures 14 and 15 (Run GW1) suggest similar temperature gradients on each side of the cuvette. The divergence in slopes in Figures 16 and 17 (Run GW3) likewise suggest that there is a slight difference in the temperature gradients from one side to the other.

6.1.2 GSRP 1 g_e Solidification Runs

A composite image for one of the ground based solidification experiments (right side of Run GS5), is shown in Figure 18. The results of the Fourier transform analysis in producing refractive index and concentration profiles for each of the ground based solidification runs are shown in Figures 19,20,21, and 22. These correspond to Runs GS4,GS5,GS6 and GS8 respectively. Each figure contains profiles for two columns within the cuvette, approximately 2.5 mm from each side. Raw data from the Fourier transform analysis method for the GSRP 1 g_e solidification runs is given in Appendix B2.

For these experiments, the actual concentration profiles are desired since concentration within the liquid plays a significant role in the solidification process and knowing how this concentration is distributed is important. As discussed previously, however, a fringe pattern analysis scheme will only give changes in phase which can then only be related to a change in refractive index and concentration. In order to tie the concentration profile onto a plot of actual concentration vs. height (i.e. C(x) rather than

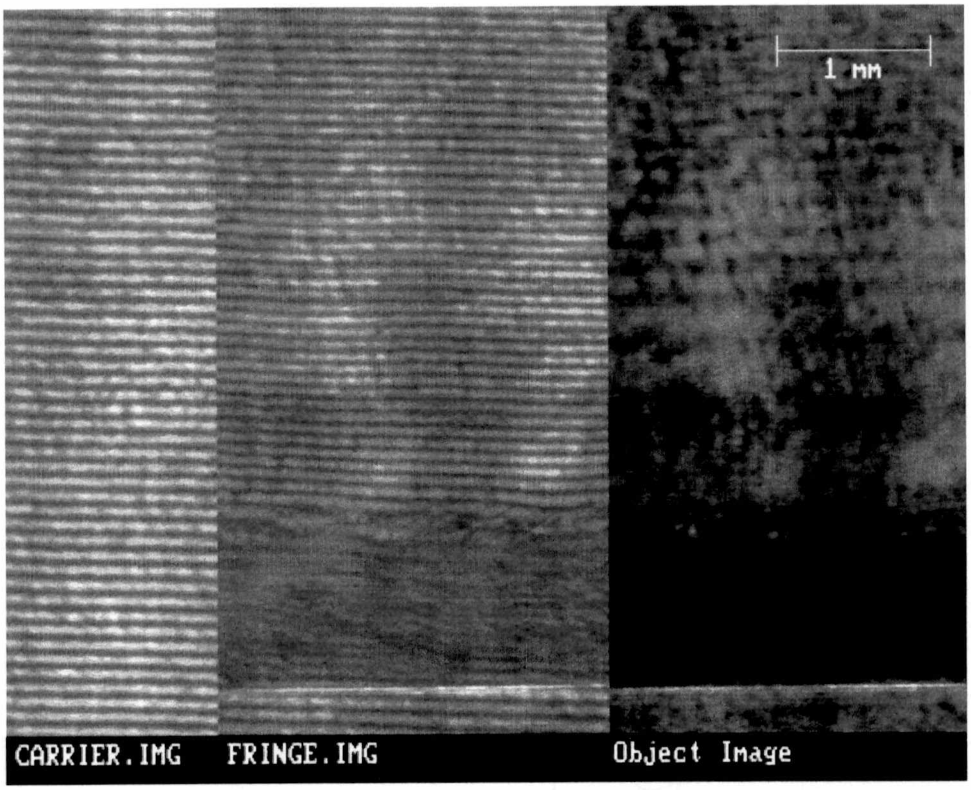

Figure 18 : Composite image for GSRP 1 g_e solidification Run GS5.

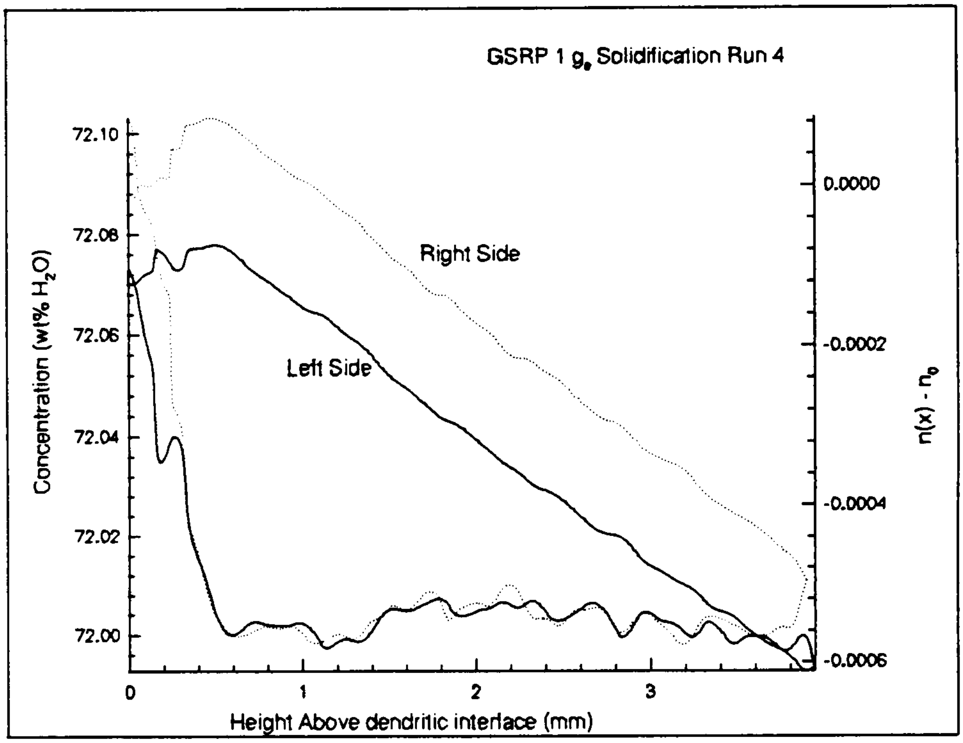

Figure 19 : Index of refraction and concentration profiles for GSRP 1 g_e solidification Run GS4.

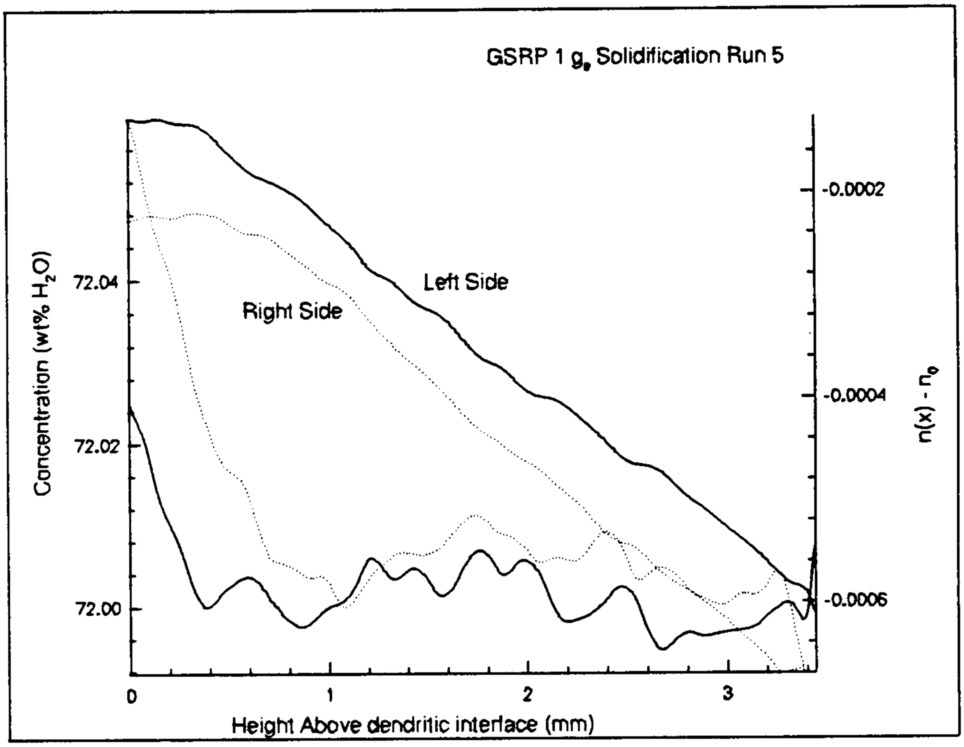

Figure 20 : Index of refraction and concentration profiles for GSRP 1 g_e solidification Run GS5.

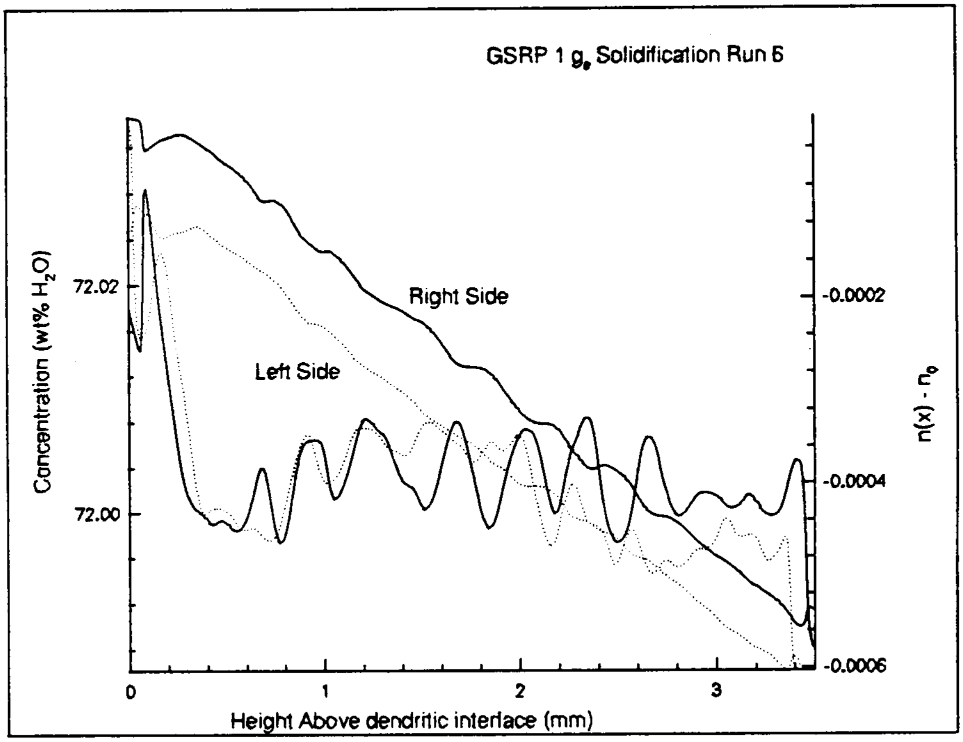

Figure 21 : Index of refraction and concentration profiles for GSRP 1 g_e solidification Run GS6.

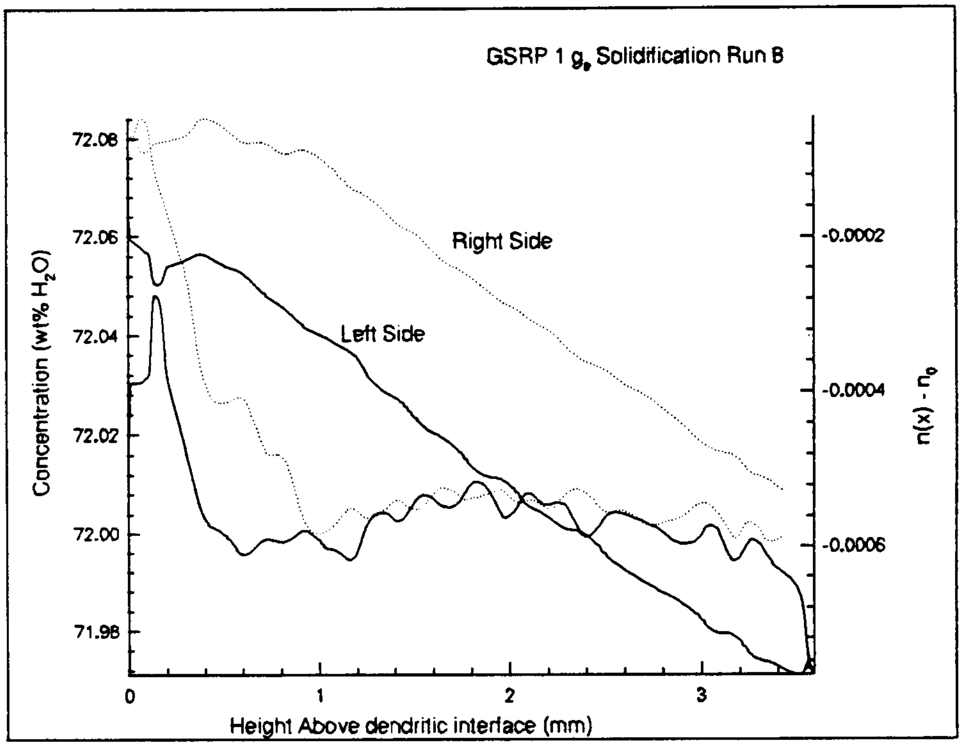

Figure 22 : Index of refraction and concentration profiles for GSRP 1 g_e solidification Run GS8.

$\Delta C(x)$), a boundary condition is required.

For the solidification of ammonium chloride under diffusion limited conditions (i.e. no convection) and assuming that the characteristic length of the concentration profile is smaller than the cuvette (so that the top of the cuvette does not influence the growth process), the concentration profile, C(x), must approach the initial bulk concentration, C_0, at some distance from the interface. This is the boundary condition selected to shift $\Delta C(x)$ along the vertical axis to produce an actual C(x) plot.

6.1.3 CAST μg_e Solidification Runs

Figure 23 is a composite of the carrier fringe pattern image, experimental fringe pattern image, and object image, for CAST μg_e solidification Run CS8 (16 minutes into the temperature ramp). These images are typical of the images from the microgravity experiments. Figures 24, 25, 26, and 27 depict the index of refraction and concentration profiles for the microgravity experiments. Three columns within each recorded hologram were studied (instead of just two, as was the case with the GSRP experiments), corresponding to the left, middle, and right most portions of the cuvette. Raw data from the Fourier transform analysis method is given in Appendix B3.

6.2 Comparison Between the Fourier Transform and Intensity Methods

The intensity method of fringe pattern analysis was applied to two holograms of the GSRP water runs and two holograms of the 1 g_e solidification runs. For the water run holograms (holograms 1-1 and 3-4), the resulting index of refraction profiles are shown

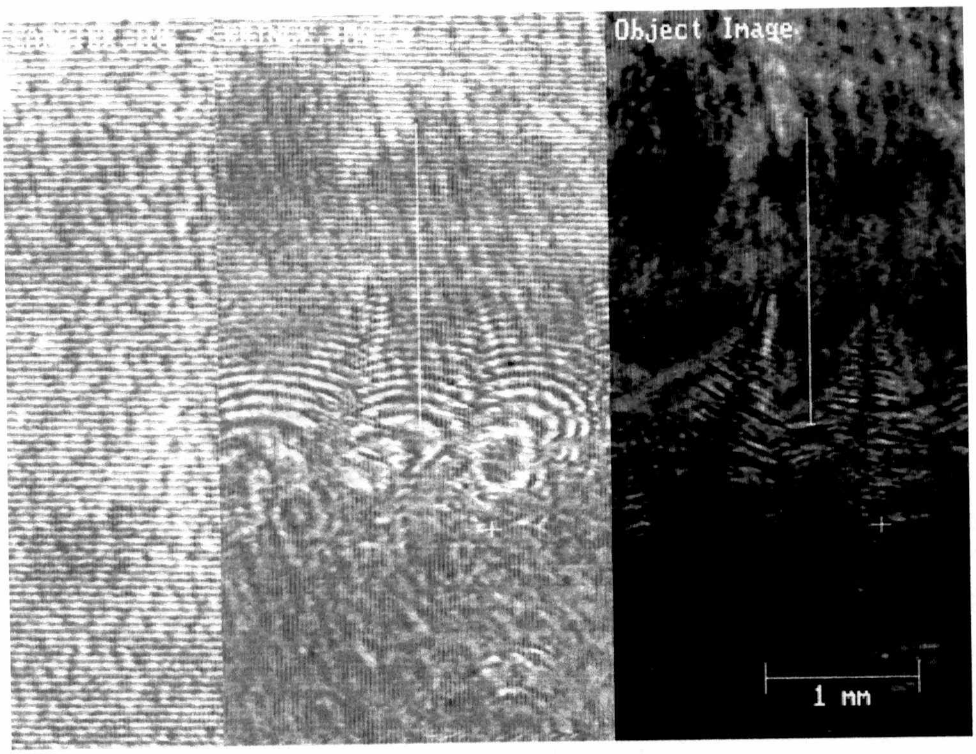

Figure 23 : Composite image of CAST μg_e solidification Run CS8 (16 minutes into the temperature ramp).

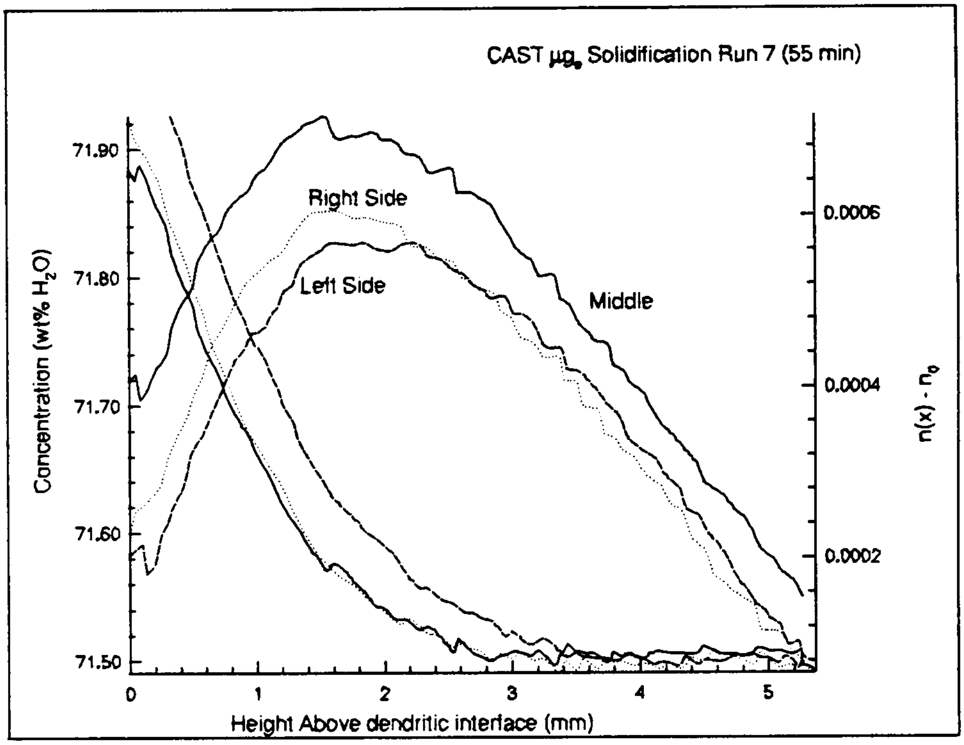

Figure 24 : Index of refraction and concentration profiles for CAST μg$_e$ solidification Run CS7 (55 minutes into temperature ramp).

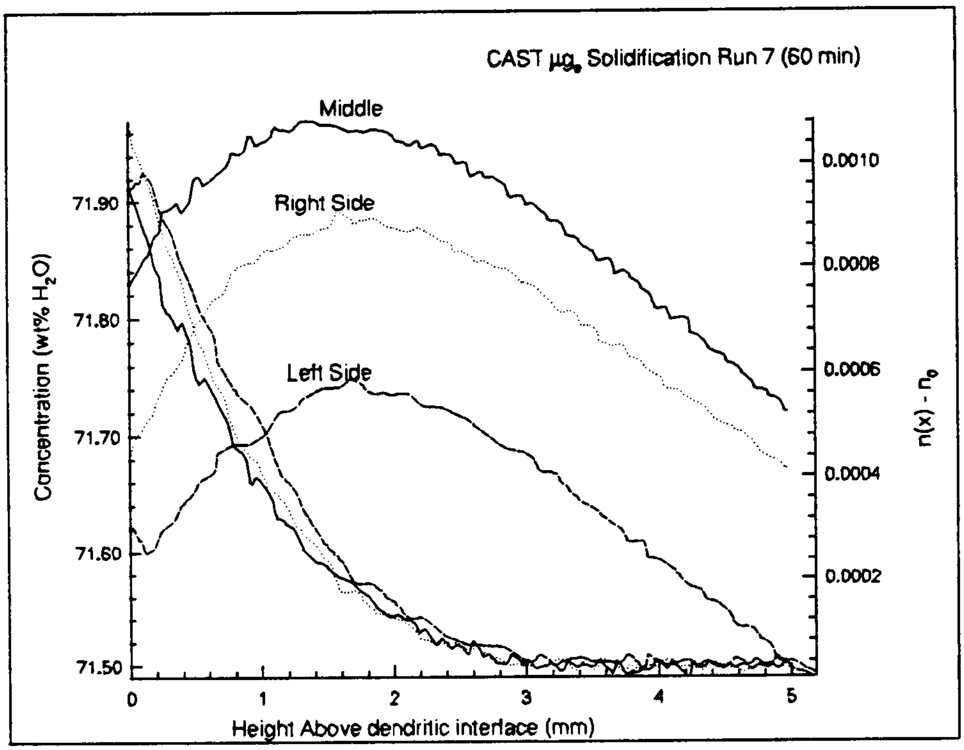

Figure 25 : Index of refraction and concentration profiles for CAST μg_e solidification Run CS7 (60 minutes into temperature ramp).

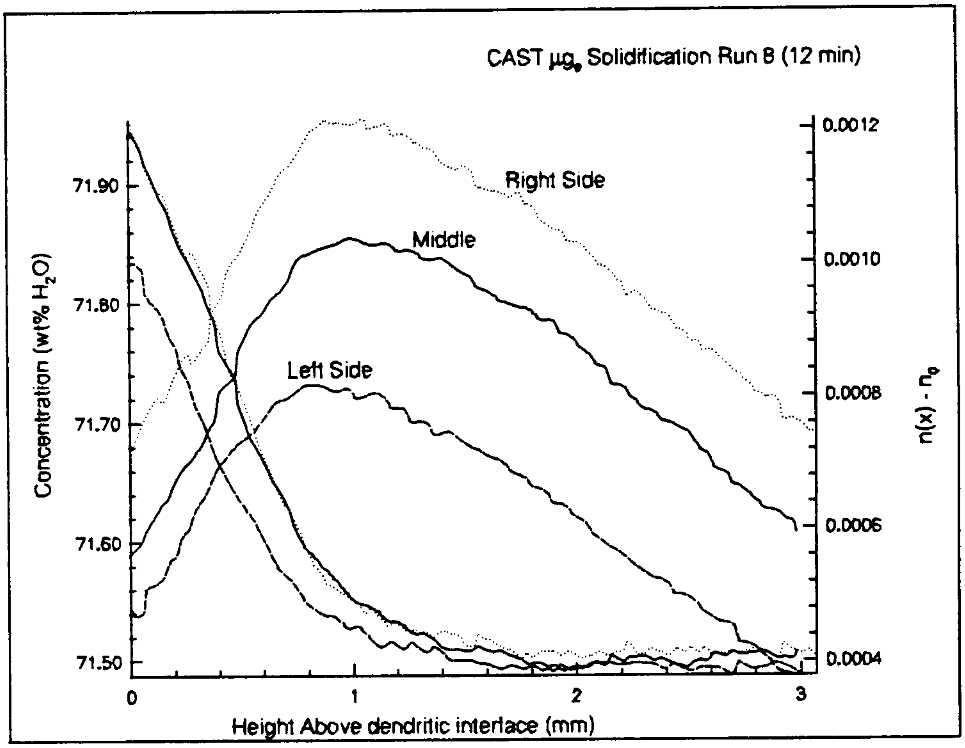

Figure 26 : Index of refraction and concentration profiles for CAST μg$_e$ solidification Run CS8 (12 minutes into temperature ramp).

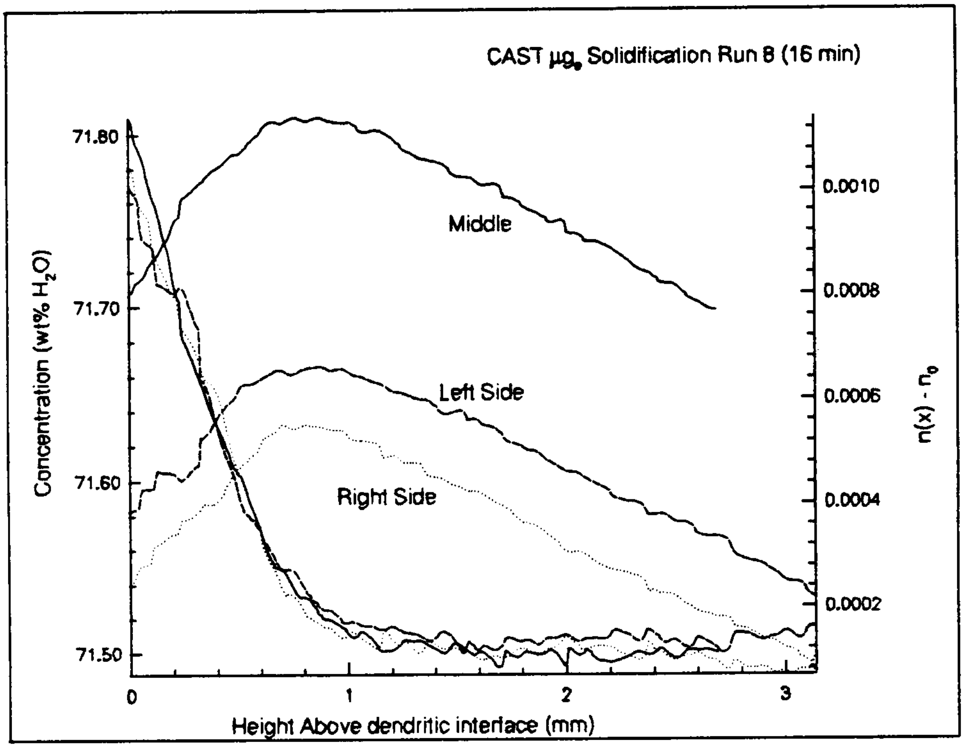

Figure 27 : Index of refraction and concentration profiles for CAST μg$_e$ solidification Run CS8 (16 minutes into temperature ramp).

in Figures 28 and 29 along with the corresponding profiles from the Fourier transform method. There is very good agreement between the shapes of the refractive index curves produced by the intensity method with those produced by the Fourier transform method.

This is likewise the case with the solidification runs (Runs GS4 and GS8), where the index of refraction profiles are shown in Figures 30 and 31, respectively, and their corresponding concentration profiles are shown in Figures 32 and 33. It must be remembered that, in the case of the refractive index curves, no attempt to place $\Delta n(x)$ on a specific location on the vertical axis has been made. Reasons for why the concentration distributions calculated using the Fourier transform method to not approach C_0 above the interface are discussed in the last chapter.

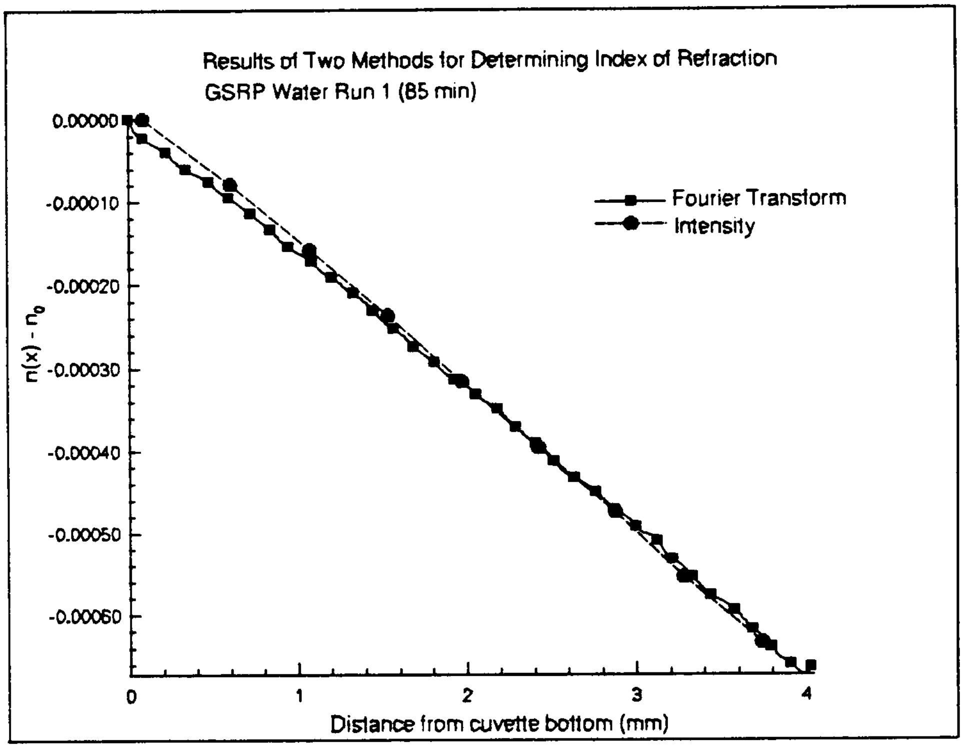

Figure 28 : A comparison between the intensity and Fourier transform methods of data reduction in measuring one of the index of refraction profiles (GSRP water Run GW1).

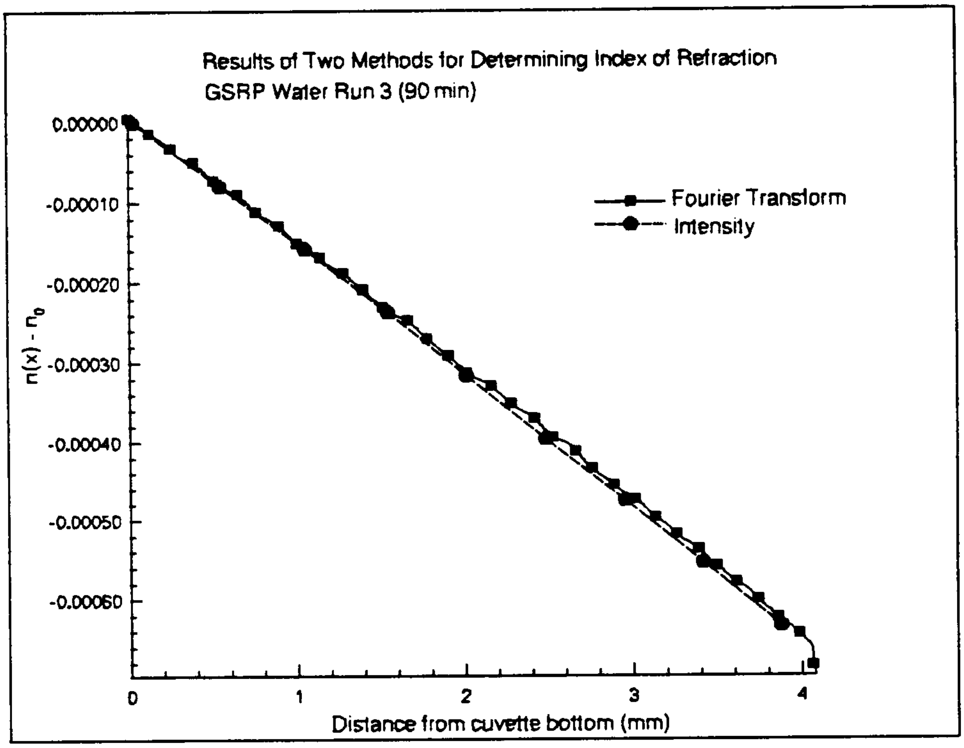

Figure 29 : A comparison between the intensity and Fourier transform methods of data reduction in measuring one of the index of refraction profiles (GSRP water Run GW3).

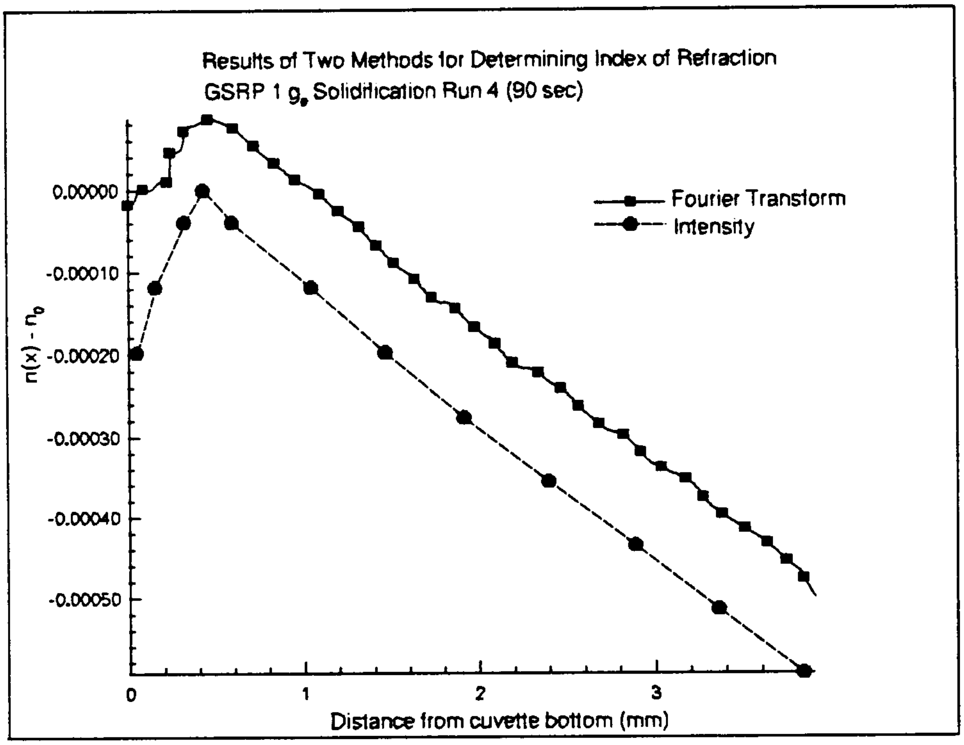

Figure 30 : A comparison between the intensity and Fourier transform methods of data reduction in measuring one of the index of refraction profiles (GSRP 1 g solidification Run GS4).

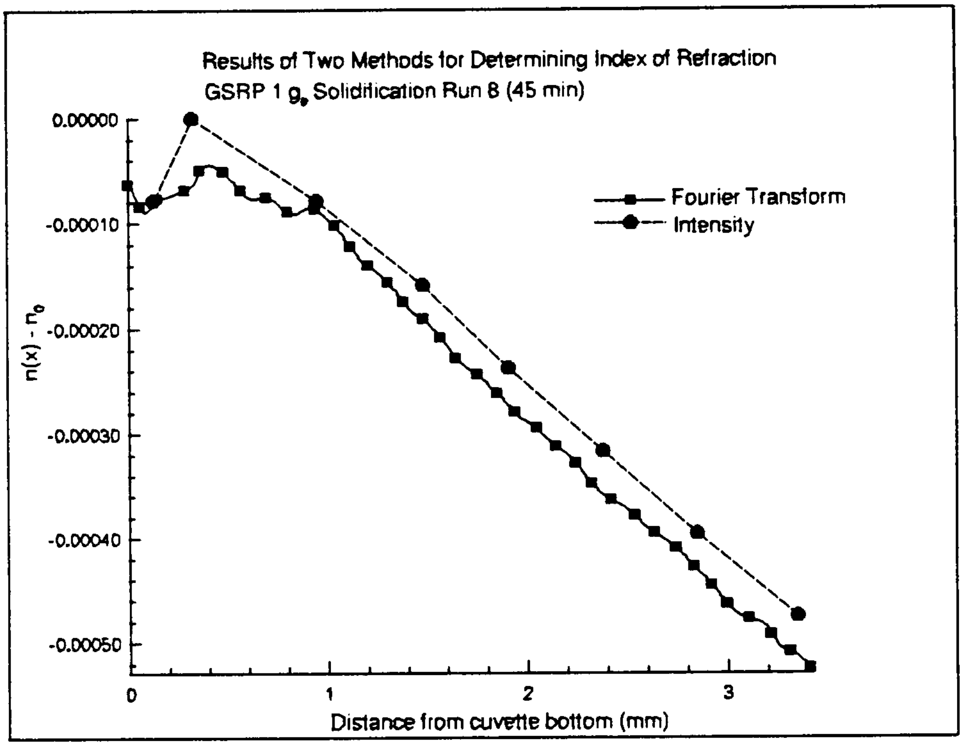

Figure 31 : A comparison between the intensity and Fourier transform methods of data reduction in measuring one of the index of refraction profiles (GSRP 1 g_e solidification Run GS8).

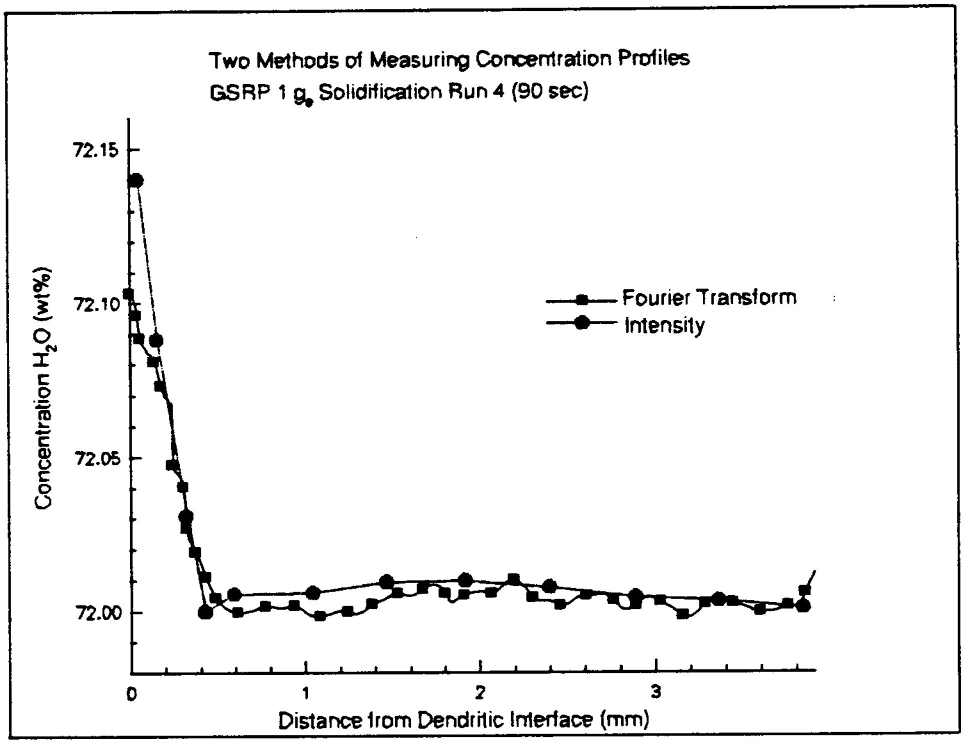

Figure 32 : A comparison between the intensity and Fourier transform methods of data reduction in measuring one of the concentration profiles (GSRP 1 g_e solidification Run GS4). These distributions were created using the index of refraction profiles shown in Figure 30.

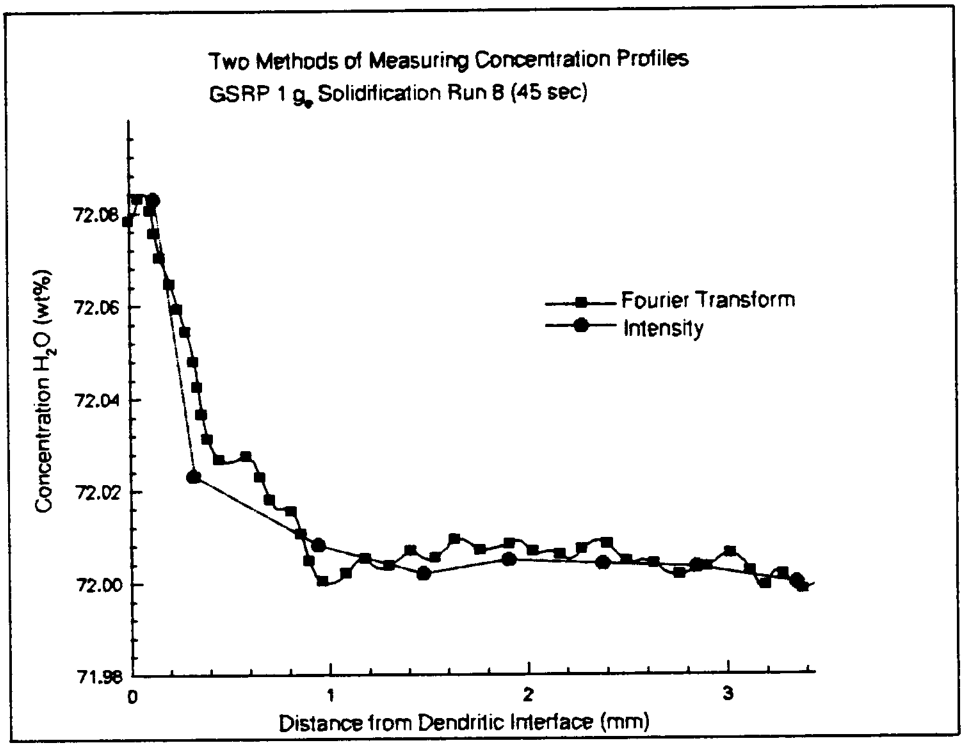

Figure 33 : A comparison between the intensity and Fourier transform methods of data reduction in measuring one of the concentration profiles (GSRP 1 g_e solidification Run GS8). These distributions were created using the index of refraction profiles shown in Figure 31.

Chapter 7 Conclusions

7.1 Results

Holography can be an effective optical tool when combined with interferometry in the study of alloy solidification and it has the potential to increase the amount data that can be extracted from an experiment performed in an environment not conducive to multiple optical processing tools (microgravity for example). By recording data at specific times, different optical processors can be applied to the reconstructed hologram as if they were applied to the original experiment. The reconstruction process takes place in a laboratory, a less demanding environment than the hologram may have been recorded in.

In its application to the study of NH_4Cl-H_2O, holography with interferometry has been shown to give 1D refractive index and concentration profiles that fit expected profiles, both in 1 g_e and μg_e conditions. These profiles were found to be comparable using two independent fringe pattern analysis schemes.

The results of Chapter 6 show that holography can record a transient solidification system for analysis at a later time. The refractive index profiles of the solidification experiments clearly indicate peaks that suggest areas of maximum density, an observed phenomena responsible for convection in the fluid during solidification in a gravity field. Concentration profiles have an exponential decay appearance away from the interface, which is the solution to the theoretical, steady state, solute distribution differential equation (Flemings, 1974).

While steady state is never actually achieved in any of the solidification experiments, the exponential solution does represent the limit these experiments approach. The microgravity experiments approximate an exponential solute distribution much better than the ground based ones, although this comparison is unfair since convection disrupts the 1 g_e profiles long before they ever approach steady state.

The results of the intensity method compare favorably with those of the Fourier transform. However, while the results are similar, their ease of use is not. The Fourier transform method is usually a faster means of extracting the phase distribution, owing to its large degree of automation. However, the added carrier frequency removes the qualitative nature of the fringe patterns, and the procedure often requires multiple attempts selecting the bandpass cutoff frequencies. This slows the process significantly. The intensity method on the other hand, is very simple to apply and the fringe pattern gives both qualitative and quantitative information. However, the subjectivity in manually identifying fringe extrema generates its own uncertainty. Also, the intensity method, on average, takes longer to apply since an individual has to assign phase values to each fringe extrema by hand. For most of the time, the Fourier transform method is faster and more efficient in extracting phase than the intensity method. However, when the Fourier transform method does not do an effective job, the intensity method can be used as an alternative.

7.2 Sources of Error

There are several sources of error in producing concentration profiles from holograms. Each of the various stages (holography, inteferometry, fringe pattern analysis, and phase to concentration conversion) has its own uncertainty that must be considered.

First, the quality of the recorded hologram is not ideal. The reconstructed object beam is not actually identical to the original object beam, and has significant noise. The Fourier transform method removes some of this effect; however, there is still a large amount of loss within the hologram.

Second, the interferometer actually measures the difference in phase between the reference and object beams. The path lengths for each of the beams are nearly the same; the only assumed difference being the phase shift introduced by the cuvette and solution in the object beam. The two beams do traverse different paths spatially and it may be that the difference in phase between the two beams has contributions from other than the cuvette and solution.

Third, since only the phase shift due to the solution is used to extract concentration distributions, the phase shift due to the cuvette was neglected and there are some valid reasons for this assumption. The cuvettes selected for the flight experiment were initially subjected to interferometry to differentiate between ones with significant phase changes in the regions of interest from those that were relatively free of phase changes. In this manner, the cuvettes used in the flight experiments were the "best" available. Subsequent reconstruction of holograms of the cuvettes without any thermal or solutal gradients suggest that the cuvettes do not play as significant a role in the formation of fringes as do the gradients themselves.

The cuvette used in each of the GSRP experiments was selected in the same manner. While, the GSRP cuvette is not as good as those used in the CAST experiments, the cuvette phase is still relatively small in comparison with the phase changes introduced by the temperature and concentration gradients. For these reasons, the assumption that the cuvette does not play a significant factor in affecting observed fringe patterns is considered reasonably valid.

A fourth source of error is in the fringe pattern analysis stage. The Fourier transform method removes alot of the subjective error associated with examining fringes using the intensity method, but it introduces other errors as well. Spectral overlap between the different peaks in the frequency domain, for example, places a fundamental limit on how well the bandpass filter can isolate the desired peak.

Finally, the index of refraction for aqueous ammonium chloride is not known accurately for a wide variety of concentrations and temperatures. An experimentally determined relation (McCay et al., 1994), considered valid near room temperature and 72 wt % H O concentration, was used to extract concentration from the index of refraction profile, however even this relation is only an approximation.

Of all these, this last is considered the largest source of error. The quality of the holograms, phase contribution of the cuvette, and uncertainty in the fringe pattern analysis methods also contribute, but by far the results are influenced the greatest by the uncertainty in the relationship between index of refraction, temperature, and concentration.

7.3 Future Work

There are a number of areas for future work related to this project. A method of accurately removing the cuvette's phase distribution from the fringe pattern could be researched. While the cuvettes used in this project can be qualitatively neglected as major contributors to the interference fringes, this will not always be true. A general, all purpose method for isolating the desired effects on interference fringes is needed. One method might be to modify the Fourier transform software so that subtraction of the cuvette's base phase can be made using base and experimental phases determined with independent carrier frequencies.

Additionally, a procedure to automate more fully the Fourier transform method would significantly increase the ease and speed with which data can be reduced. Currently, the selection of cutoff frequencies for filtering the fringe pattern of the experimental image requires the largest amount of time and has a large degree of subjectivity to it. The selection process entails choosing cutoff frequencies and viewing the resulting refractive index profile. If the profile does not match what is expected, a different set of cutoff frequencies is selected. The process is repeated until an "acceptable" refractive index profile is found. A procedure that is more independent of human interaction would greatly improve the data reduction process, and increase the amount of data that can be analyzed.

List of Sources

Born, M. and E. Wolf. *Principles of Optics: Electromagnetic Theory of Propogation, Interference, and Diffraction of Light (6th Ed)*. Pergamon Press: New York, 1991

Chen, C.F., and F. Chen. "Experimental Study of Directional Solidification of Aqueous Ammonium Chloride Solution". *Journal of Fluid Mechanics*. Vol 227 (1991), pp567-586.

Christenson, M.S., and F.P. Incropera. "Solidification of an Aqueous Ammonium Chloride Solution in a Rectangular Cavity - I Experimental Study". *International Journal of Heat and Mass Transfer*. Vol 32, No 1 (1989) pp 47-68 .

Copley, S.M., and A.F. Giamei, S.M.Johnson, M.F. Hornbecker. "The Origin of Freckles in Unidirectionally Solidified Castings" *Metallurgical Transactions*. Vol. 1, August 1970. 2193

Flemings, M.C. *Solidification Processing*. McGraw-Hill, New York. 1974

Gabor, D., "Microscopy by reconstructed wave-fronts". *Proc. Roy. Soc A., 197*, p454. 1949

Gabor, D., "Microscopy by reconstructed wave-fronts: II". *The Proceedings of the Physical Society, 378B* Vol. 64 Part 6, 1 June 1951. p449

Hopkins, J.A. "Experimental study of convective instability of the diffusion layer produced during directional solidification of a metal model material." M.S. Thesis, University of Tennessee, Knoxville, August 1989.

Iwasaki, A and S. Hosokawa, I. Kudo, M. Tanimoto, H. Sakurai, Y. Arai, T. Watanabe, S. Kawai, M. Ishikawa, S. Kamei. "Visualization of a solidification process in microgravity" *Journal of Thermophysics and Heat Transfer* Vol. 6 no 4 Oct-Dec 1992 p 733

Johnston, M.H., and C.S. Griner, R.A. Parr, S.J. Robertson "The direct observation of unidirectional solidification as a function of gravity level:. *Journal of Crystal Growth*. Vol. 50 1980 pp 831-838

Johnston, M.H. and R.B. Owen, R.E. Shurney "Optical Observations of Unidirectional Solidification in microgravity" NASA Technical paper 2110, Jan 1983.

Kurz, W. and D.J. Fisher. *Fundamentals of Solidification* (Trans Tech Publications) 1989. Aedermannsdorf. Switzerland.

Mach, L. *Zeitschr.f.,Instrkde*, 12 (1892), 89.

Magnani, M.E. "Fourier-transform Method to Measure Concentration during Solidification of a Transparent Metal Model." M.S. Thesis. University of Tennessee, Knoxville. December 1991.

McCay, M.H. and V. Semak, J. Hopkins. "Index of Refraction of Ammonium Chloride-Water as a Function of Wavelength". Submitted for publication. (1994).

McCay, T.D. and M.H. McCay. "Measured and Predicted Effects of Gravity Level on Directional Solidification of NH_4Cl-H_2O". Microgravity Sci. Technol. VI/1 (1993).

McCay, T.D. and J.A. Hopkins, M.H. McCay. "Influence of gravity Level on free convection Effects during Bridgman Directional Dendritic Solidification". Paper presented at 29th National Heat Transfer Conference August 8-11, 1993, Atlanta.

McCay, T.D. and M.H. McCay, P.A. Gray. "Experimental Observation of Convective Breakdown during Directional Solidification". *Physical Review Letters*. Vol. 62 No 17 April 24 1989. p2060.

McCay, T.D., and M.H. McCay, S.A. Lowry, L.M. Smith. "Convective Instabilities During Directional Solidification". J. Thermophys Heat Transfer. 3, 345-350 (1989).

Sample, A.K., and A. Hellawell. The Mechanism of Formation and Prevention of Channel Segregation during Alloy Solidification". *Metallurgical Transactions A*. Vol. 15A December 1984 p 2163.

Zehnder, L. *Zeitschr.f.,Instrkde,* 11 (1891) 275.

APPENDICES

APPENDIX A1 - Equipment

Holographic Reconstruction System

CAST Holographic Reconstruction System with Interferometry

LASER
1 Spectra-Physics Model 127 60mW HeNe Laser

BS1 (BEAMSPLITTER)
1 Jodon Model VBA-200 Variable Beamsplitter
1 Newport Model 150 Magnetic Base

M1 (MIRROR)
1 mirror
1 Newport Model 625A-2C Mirror Mount
1 Newport Model 40 Mounting Rod
1 Newport Model 150 Magnetic Base

C1 (COLLIMATOR/SF)
1 Melles Griot Model 09LCM003 50mm Collimator
1 Melles Griot Model 09LSF011 Spatial Filter w/ 10.0 µm Model 09LSP013 Pinhole
1 Adjustable Threaded Mount
1 Newport Model 150 Magnetic Base
1 Newport Model 270 Laboratory Jack

HOLOGRAM (HOLOGRAM HOLDER)
1 Custom Designed Vacuum Hologram Holder w/ 1 Magnetek 0.62A Electric Motor
or 1 Newport Model 520 Glass Plate Holder
1 Aerotech Model ATT185-5 Tilt/Rotation Stage
1 Newport Model 430 Low Profile Translation Stage
1 Newport Model 440 Low Profile Translation Stage

M2 (MIRROR)
1 Mirror
1 Newport Model 625A-2C Mirror Mount
1 Newport Model 40 Mounting Rod
1 Newport Model 150 Magnetic Base

C1 (COLLIMATOR/SF)
1 Spectra Physics Model 336 Multiwavelength Collimator
1 Spectra Physics Model 332 Spatial Filter with Aperture A2 (4.7 μm) Pinhole
1 Newport Model TSX-1A Translation Stage
1 Newport Model 280 Laboratory Jack
Post, Post Holder, Threaded Mount

M3 (MIRROR)
1 Mirror
1 Newport 625A-4C Mirror Mount
1 Newport Model 40 Mounting Rod
1 Newport Model 430 Translation Stage
1 Newport Model 150 Magnetic Base

BS2 (BEAM SPLITTER)
1 Melles Griot Model 03BSC015 Cube Beamsplitter
1 Melles Griot Model 07TTA003 Beamsplitter Table
1 Newport Model 270 Laboratory Jack
1 Newport Model 150 Magnetic Base

L1 / L2 (IMAGING LENSES)
2 Ealing Electro-Optics Model 42-2170 500 mm Focal Length Biconvex Lenses **(L1, L2)**
2 Melles Griot Model 07LHF025 Lens Holders
2 Newport Model SP-6 Posts
2 Newport Model VPH-6 Post Holders
4 Newport Model B-2 Bases
2 Newport Model URL-36 Optical Rails

CAMERA (CAMERA ASSEMBLY)
1 Burle Model TC651E Camera
2 Newport Model SP-2 Posts
2 Newport Model VPH-2 Post Holders
1 Newport Model 440 Translation Stage
1 Newport Model 270 Laboratory Jack
1 Newport Model AMB-2 Adjustable Mounting Base
1 Neutral Density Filter (from Newport Model FS-3 ND Filter Kit)
1 Newport Model FH-1 Filter Holder

APPENDIX A2 - Equipment

Image Processing

Image Processing System

IBM PC compatible

- 486 DX2 66MHz Local Bus motherboard
- Stealth Vram Local Bus Video 1MB
- Sony Trinitron 17" SVGA Monitor (Model CPD-1604S)
- 8 MB RAM
- 256 KB External Cache
- 260 MB Hard Disk Drive
- 3.5", 5.25" Floppy Disk Drives
- Logitech Mouseman Mouse
- 101 Key AT Keyboard

DATA TRANSLATION DT2862 Image Processor (4 Memory Buffers)

- Sony Trinitron RGB Color monitor (Model PVM-1342Q)

Sony VHS Video Cassette Recorder (Model SLV-373UC)

Acer AcerLaser IIIG Grayscale Laser Printer (Model 7278-G)

APPENDIX B1 - Raw Data

GSRP Water Runs

Experiment: GSRP Water Run 1

Hologram: 1-1

1.	Horizontal Image scale (pix/mm)	82
2.	Vertical Image scale (pix/mm)	102
3.	Column for carrier image (pix)	255
4.	Lower cutoff for carrier image (pix)	52
5.	Upper cutoff for carrier image (pix)	81
6.	Carrier frequency (pix)	62.84
7.	Column for experimental image (pix)	255
8.	Cuvette bottom for experimental image (pix)	415
9.	Interface for experimental image (pix)	415
10	Distance from right side of cuvette (pix)	206
11.	Lower cutoff for experimental image (pix)	44
12.	Upper cutoff for experimental image (pix)	99
13.	Fringe to fringe distance in FRINGE.PLT (pix)	50
14.	Maximum refractive index window in N.PLT (mm)	
15.	Recommended temperature gradient (°C/cm)	14.43
16.	Concentration of water in bulk liquid (wt%)	100
17.	Tip concentration (wt%)	
18.	Final temperature gradient (°C/cm)	
19.	Final tip concentration (wt%)	

Experiment: GSRP Water Run 1

Hologram: 1-1

1.	Horizontal Image scale (pix/mm)	82
2.	Vertical Image scale (pix/mm)	102
3.	Column for carrier image (pix)	255
4.	Lower cutoff for carrier image (pix)	52
5.	Upper cutoff for carrier image (pix)	81
6.	Carrier frequency (pix)	62.84
7.	Column for experimental image (pix)	255
8.	Cuvette bottom for experimental image (pix)	415
9.	Interface for experimental image (pix)	414
10	Distance from right side of cuvette (pix)	1141
11.	Lower cutoff for experimental image (pix)	49
12.	Upper cutoff for experimental image (pix)	98
13.	Fringe to fringe distance in FRINGE.PLT (pix)	52
14.	Maximum refractive index window in N.PLT (mm)	
15.	Recommended temperature gradient (°C/cm)	13.88
16.	Concentration of water in bulk liquid (wt%)	100
17.	Tip concentration (wt%)	
18.	Final temperature gradient (°C/cm)	
19.	Final tip concentration (wt%)	

Experiment: GSRP Water Run 1

Hologram: 1-2

1.	Horizontal Image scale (pix/mm)	82
2.	Vertical Image scale (pix/mm)	102
3.	Column for carrier image (pix)	255
4.	Lower cutoff for carrier image (pix)	47
5.	Upper cutoff for carrier image (pix)	81
6.	Carrier frequency (pix)	60.18
7.	Column for experimental image (pix)	255
8.	Cuvette bottom for experimental image (pix)	431
9.	Interface for experimental image (pix)	430
10	Distance from right side of cuvette (pix)	209
11.	Lower cutoff for experimental image (pix)	47
12.	Upper cutoff for experimental image (pix)	96
13.	Fringe to fringe distance in FRINGE.PLT (pix)	55
14.	Maximum refractive index window in N.PLT (mm)	
15.	Recommended temperature gradient (°C/cm)	13.12
16.	Concentration of water in bulk liquid (wt%)	100
17.	Tip concentration (wt%)	
18.	Final temperature gradient (°C/cm)	14.5
19.	Final tip concentration (wt%)	

Experiment: GSRP Water Run 1

Hologram: 1-2

1.	Horizontal Image scale (pix/mm)	82
2.	Vertical Image scale (pix/mm)	102
3.	Column for carrier image (pix)	255
4.	Lower cutoff for carrier image (pix)	47
5.	Upper cutoff for carrier image (pix)	81
6.	Carrier frequency (pix)	60.18
7.	Column for experimental image (pix)	255
8.	Cuvette bottom for experimental image (pix)	426
9.	Interface for experimental image (pix)	425
10	Distance from right side of cuvette (pix)	1091
11.	Lower cutoff for experimental image (pix)	49
12.	Upper cutoff for experimental image (pix)	98
13.	Fringe to fringe distance in FRINGE.PLT (pix)	53
14.	Maximum refractive index window in N.PLT (mm)	
15.	Recommended temperature gradient (°C/cm)	13.62
16.	Concentration of water in bulk liquid (wt%)	100
17.	Tip concentration (wt%)	
18.	Final temperature gradient (°C/cm)	15
19.	Final tip concentration (wt%)	

Experiment: GSRP Water Run 3

Hologram: 3-4

1.	Horizontal Image scale (pix/mm)	82
2.	Vertical Image scale (pix/mm)	102
3.	Column for carrier image (pix)	255
4.	Lower cutoff for carrier image (pix)	32
5.	Upper cutoff for carrier image (pix)	78
6.	Carrier frequency (pix)	52.86
7.	Column for experimental image (pix)	255
8.	Cuvette bottom for experimental image (pix)	426
9.	Interface for experimental image (pix)	418
10	Distance from right side of cuvette (pix)	222
11.	Lower cutoff for experimental image (pix)	35
12.	Upper cutoff for experimental image (pix)	100
13.	Fringe to fringe distance in FRINGE.PLT (pix)	51
14.	Maximum refractive index window in N.PLT (mm)	
15.	Recommended temperature gradient (°C/cm)	14.15
16.	Concentration of water in bulk liquid (wt%)	100
17.	Tip concentration (wt%)	
18.	Final temperature gradient (°C/cm)	13
19.	Final tip concentration (wt%)	

Experiment: GSRP Water Run 3

Hologram: 3-4

1.	Horizontal Image scale (pix/mm)	82
2.	Vertical Image scale (pix/mm)	102
3.	Column for carrier image (pix)	255
4.	Lower cutoff for carrier image (pix)	32
5.	Upper cutoff for carrier image (pix)	78
6.	Carrier frequency (pix)	52.86
7.	Column for experimental image (pix)	255
8.	Cuvette bottom for experimental image (pix)	408
9.	Interface for experimental image (pix)	407
10	Distance from right side of cuvette (pix)	1097
11.	Lower cutoff for experimental image (pix)	39
12.	Upper cutoff for experimental image (pix)	92
13.	Fringe to fringe distance in FRINGE.PLT (pix)	69
14.	Maximum refractive index window in N.PLT (mm)	
15.	Recommended temperature gradient (°C/cm)	10.46
16.	Concentration of water in bulk liquid (wt%)	100
17.	Tip concentration (wt%)	
18.	Final temperature gradient (°C/cm)	
19.	Final tip concentration (wt%)	

Experiment: GSRP Water Run 3

Hologram: 3-5

1.	Horizontal Image scale (pix/mm)	82
2.	Vertical Image scale (pix/mm)	102
3.	Column for carrier image (pix)	255
4.	Lower cutoff for carrier image (pix)	47
5.	Upper cutoff for carrier image (pix)	82
6.	Carrier frequency (pix)	63.76
7.	Column for experimental image (pix)	255
8.	Cuvette bottom for experimental image (pix)	418
9.	Interface for experimental image (pix)	417
10	Distance from right side of cuvette (pix)	214
11.	Lower cutoff for experimental image (pix)	36
12.	Upper cutoff for experimental image (pix)	112
13.	Fringe to fringe distance in FRINGE.PLT (pix)	62
14.	Maximum refractive index window in N.PLT (mm)	
15.	Recommended temperature gradient (°C/cm)	11.64
16.	Concentration of water in bulk liquid (wt%)	100
17.	Tip concentration (wt%)	
18.	Final temperature gradient (°C/cm)	
19.	Final tip concentration (wt%)	

Experiment: GSRP Water Run 3

Hologram: Hologram 3-5

1.	Horizontal Image scale (pix/mm)	82
2.	Vertical Image scale (pix/mm)	102
3.	Column for carrier image (pix)	255
4.	Lower cutoff for carrier image (pix)	47
5.	Upper cutoff for carrier image (pix)	82
6.	Carrier frequency (pix)	63.76
7.	Column for experimental image (pix)	255
8.	Cuvette bottom for experimental image (pix)	431
9.	Interface for experimental image (pix)	430
10	Distance from right side of cuvette (pix)	1077
11.	Lower cutoff for experimental image (pix)	47
12.	Upper cutoff for experimental image (pix)	99
13.	Fringe to fringe distance in FRINGE.PLT (pix)	69
14.	Maximum refractive index window in N.PLT (mm)	
15.	Recommended temperature gradient (°C/cm)	10.46
16.	Concentration of water in bulk liquid (wt%)	100
17.	Tip concentration (wt%)	
18.	Final temperature gradient (°C/cm)	
19.	Final tip concentration (wt%)	

APPENDIX B2 - Raw Data

GSRP 1 g_e Solidification Runs

Experiment: GSRP 1 ge Solidification Run 4

Hologram: 4

1.	Horizontal Image scale (pix/mm)	82
2.	Vertical Image scale (pix/mm)	102
3.	Column for carrier image (pix)	255
4.	Lower cutoff for carrier image (pix)	48
5.	Upper cutoff for carrier image (pix)	90
6.	Carrier frequency (pix)	65.41
7.	Column for experimental image (pix)	207
8.	Cuvette bottom for experimental image (pix)	443
9.	Interface for experimental image (pix)	400
10	Distance from right side of cuvette (pix)	272
11.	Lower cutoff for experimental image (pix)	52
12.	Upper cutoff for experimental image (pix)	111
13.	Fringe to fringe distance in FRINGE.PLT (pix)	52
14.	Maximum refractive index window in N.PLT (mm)	.6
15.	Recommended temperature gradient (°C/cm)	13.88
16.	Concentration of water in bulk liquid (wt%)	72
17.	Tip concentration (wt%)	72.10
18.	Final temperature gradient (°C/cm)	15.0
19.	Final tip concentration (wt%)	72.10

Experiment: GSRP 1 ge Solidification Run 4

Hologram: 4

1.	Horizontal Image scale (pix/mm)	82
2.	Vertical Image scale (pix/mm)	102
3.	Column for carrier image (pix)	255
4.	Lower cutoff for carrier image (pix)	48
5.	Upper cutoff for carrier image (pix)	90
6.	Carrier frequency (pix)	65.41
7.	Column for experimental image (pix)	337
8.	Cuvette bottom for experimental image (pix)	449
9.	Interface for experimental image (pix)	404
10	Distance from right side of cuvette (pix)	997
11.	Lower cutoff for experimental image (pix)	53
12.	Upper cutoff for experimental image (pix)	101
13.	Fringe to fringe distance in FRINGE.PLT (pix)	50
14.	Maximum refractive index window in N.PLT (mm)	.64
15.	Recommended temperature gradient (°C/cm)	14.43
16.	Concentration of water in bulk liquid (wt%)	72
17.	Tip concentration (wt%)	72.07
18.	Final temperature gradient (°C/cm)	
19.	Final tip concentration (wt%)	

Experiment: GSRP 1 ge Solidification Run 5

Hologram: 5

1.	Horizontal Image scale (pix/mm)	82
2.	Vertical Image scale (pix/mm)	102
3.	Column for carrier image (pix)	255
4.	Lower cutoff for carrier image (pix)	33
5.	Upper cutoff for carrier image (pix)	78
6.	Carrier frequency (pix)	52.83
7.	Column for experimental image (pix)	97
8.	Cuvette bottom for experimental image (pix)	443
9.	Interface for experimental image (pix)	347
10	Distance from right side of cuvette (pix)	372
11.	Lower cutoff for experimental image (pix)	43
12.	Upper cutoff for experimental image (pix)	87
13.	Fringe to fringe distance in FRINGE.PLT (pix)	52
14.	Maximum refractive index window in N.PLT (mm)	.46
15.	Recommended temperature gradient (°C/cm)	13.88
16.	Concentration of water in bulk liquid (wt%)	72
17.	Tip concentration (wt%)	72.04
18.	Final temperature gradient (°C/cm)	15.0
19.	Final tip concentration (wt%)	72.04

Experiment: GSRP ! ge Solidification Run 5

Hologram: 5

1.	Horizontal Image scale (pix/mm)	82
2.	Vertical Image scale (pix/mm)	102
3.	Column for carrier image (pix)	255
4.	Lower cutoff for carrier image (pix)	33
5.	Upper cutoff for carrier image (pix)	78
6.	Carrier frequency (pix)	52.83
7.	Column for experimental image (pix)	284
8.	Cuvette bottom for experimental image (pix)	449
9.	Interface for experimental image (pix)	353
10	Distance from right side of cuvette (pix)	1056
11.	Lower cutoff for experimental image (pix)	44
12.	Upper cutoff for experimental image (pix)	83
13.	Fringe to fringe distance in FRINGE.PLT (pix)	62
14.	Maximum refractive index window in N.PLT (mm)	.40
15.	Recommended temperature gradient (°C/cm)	11.64
16.	Concentration of water in bulk liquid (wt%)	72
17.	Tip concentration (wt%)	72.02
18.	Final temperature gradient (°C/cm)	13.5
19.	Final tip concentration (wt%)	72.02

Experiment: GSRP 1 ge Solidification Run 6

Hologram: 6

1.	Horizontal Image scale (pix/mm)	82
2.	Vertical Image scale (pix/mm)	102
3.	Column for carrier image (pix)	255
4.	Lower cutoff for carrier image (pix)	30
5.	Upper cutoff for carrier image (pix)	77
6.	Carrier frequency (pix)	54.79
7.	Column for experimental image (pix)	179
8.	Cuvette bottom for experimental image (pix)	440
9.	Interface for experimental image (pix)	351
10	Distance from right side of cuvette (pix)	293
11.	Lower cutoff for experimental image (pix)	41
12.	Upper cutoff for experimental image (pix)	96
13.	Fringe to fringe distance in FRINGE.PLT (pix)	53
14.	Maximum refractive index window in N.PLT (mm)	.42
15.	Recommended temperature gradient (°C/cm)	13.62
16.	Concentration of water in bulk liquid (wt%)	72
17.	Tip concentration (wt%)	
18.	Final temperature gradient (°C/cm)	14.5
19.	Final tip concentration (wt%)	72.03

Experiment: GSRP 1 ge Solidification Run 6

Hologram: 6

1.	Horizontal Image scale (pix/mm)	82
2.	Vertical Image scale (pix/mm)	102
3.	Column for carrier image (pix)	255
4.	Lower cutoff for carrier image (pix)	30
5.	Upper cutoff for carrier image (pix)	77
6.	Carrier frequency (pix)	54.79
7.	Column for experimental image (pix)	232
8.	Cuvette bottom for experimental image (pix)	449
9.	Interface for experimental image (pix)	359
10	Distance from right side of cuvette (pix)	1113
11.	Lower cutoff for experimental image (pix)	42
12.	Upper cutoff for experimental image (pix)	89
13.	Fringe to fringe distance in FRINGE.PLT (pix)	57
14.	Maximum refractive index window in N.PLT (mm)	.38
15.	Recommended temperature gradient (°C/cm)	12.66
16.	Concentration of water in bulk liquid (wt%)	72
17.	Tip concentration (wt%)	72.02
18.	Final temperature gradient (°C/cm)	15.0
19.	Final tip concentration (wt%)	72.02

Experiment: GSRP 1 ge Solidification Run 8

Hologram: 8

1.	Horizontal Image scale (pix/mm)	82
2.	Vertical Image scale (pix/mm)	102
3.	Column for carrier image (pix)	255
4.	Lower cutoff for carrier image (pix)	34
5.	Upper cutoff for carrier image (pix)	77
6.	Carrier frequency (pix)	53.58
7.	Column for experimental image (pix)	124
8.	Cuvette bottom for experimental image (pix)	449
9.	Interface for experimental image (pix)	352
10	Distance from right side of cuvette (pix)	359
11.	Lower cutoff for experimental image (pix)	39
12.	Upper cutoff for experimental image (pix)	97
13.	Fringe to fringe distance in FRINGE.PLT (pix)	42
14.	Maximum refractive index window in N.PLT (mm)	.49
15.	Recommended temperature gradient (°C/cm)	17.18
16.	Concentration of water in bulk liquid (wt%)	72
17.	Tip concentration (wt%)	72.06
18.	Final temperature gradient (°C/cm)	16
19.	Final tip concentration (wt%)	72.05

Experiment: GSRP 1 ge Soldification Run 8

Hologram: 8

1.	Horizontal Image scale (pix/mm)	82
2.	Vertical Image scale (pix/mm)	102
3.	Column for carrier image (pix)	255
4.	Lower cutoff for carrier image (pix)	34
5.	Upper cutoff for carrier image (pix)	77
6.	Carrier frequency (pix)	53.58
7.	Column for experimental image (pix)	342
8.	Cuvette bottom for experimental image (pix)	452
9.	Interface for experimental image (pix)	368
10	Distance from right side of cuvette (pix)	991
11.	Lower cutoff for experimental image (pix)	41
12.	Upper cutoff for experimental image (pix)	96
13.	Fringe to fringe distance in FRINGE.PLT (pix)	48
14.	Maximum refractive index window in N.PLT (mm)	.5
15.	Recommended temperature gradient (°C/cm)	15.03
16.	Concentration of water in bulk liquid (wt%)	72
17.	Tip concentration (wt%)	
18.	Final temperature gradient (°C/cm)	
19.	Final tip concentration (wt%)	

APPENDIX B3 - Raw Data

CAST μg_c Solidification Runs

Experiment: CAST mge Solidifcation Run 7

Hologram: 296

1.	Horizontal Image scale (pix/mm)	48
2.	Vertical Image scale (pix/mm)	60
3.	Column for carrier image (pix)	200
4.	Lower cutoff for carrier image (pix)	61
5.	Upper cutoff for carrier image (pix)	103
6.	Carrier frequency (pix)	78.86
7.	Column for experimental image (pix)	165
8.	Cuvette bottom for experimental image (pix)	480
9.	Interface for experimental image (pix)	324
10	Distance from right side of cuvette (pix)	631
11.	Lower cutoff for experimental image (pix)	40
12.	Upper cutoff for experimental image (pix)	110
13.	Fringe to fringe distance in FRINGE.PLT (pix)	26
14.	Maximum refractive index window in N.PLT (mm)	1.8
15.	Recommended temperature gradient (°C/cm)	16.33
16.	Concentration of water in bulk liquid (wt%)	71.5
17.	Tip concentration (wt%)	71.87
18.	Final temperature gradient (°C/cm)	
19.	Final tip concentration (wt%)	

Experiment: CAST mge Solidification Run 7

Hologram: 296

1.	Horizontal Image scale (pix/mm)	48
2.	Vertical Image scale (pix/mm)	60
3.	Column for carrier image (pix)	200
4.	Lower cutoff for carrier image (pix)	61
5.	Upper cutoff for carrier image (pix)	103
6.	Carrier frequency (pix)	78.86
7.	Column for experimental image (pix)	279
8.	Cuvette bottom for experimental image (pix)	480
9.	Interface for experimental image (pix)	318
10	Distance from right side of cuvette (pix)	517
11.	Lower cutoff for experimental image (pix)	40
12.	Upper cutoff for experimental image (pix)	119
13.	Fringe to fringe distance in FRINGE.PLT (pix)	26
14.	Maximum refractive index window in N.PLT (mm)	1.833
15.	Recommended temperature gradient (°C/cm)	16.33
16.	Concentration of water in bulk liquid (wt%)	71.5
17.	Tip concentration (wt%)	71.83
18.	Final temperature gradient (°C/cm)	
19.	Final tip concentration (wt%)	

Experiment: CAST mge Solidification Run 7

Hologram: 296

1.	Horizontal Image scale (pix/mm)	48
2.	Vertical Image scale (pix/mm)	60
3.	Column for carrier image (pix)	200
4.	Lower cutoff for carrier image (pix)	61
5.	Upper cutoff for carrier image (pix)	103
6.	Carrier frequency (pix)	78.86
7.	Column for experimental image (pix)	237
8.	Cuvette bottom for experimental image (pix)	480
9.	Interface for experimental image (pix)	337
10	Distance from right side of cuvette (pix)	242
11.	Lower cutoff for experimental image (pix)	40
12.	Upper cutoff for experimental image (pix)	133
13.	Fringe to fringe distance in FRINGE.PLT (pix)	24
14.	Maximum refractive index window in N.PLT (mm)	2.53
15.	Recommended temperature gradient (°C/cm)	17.69
16.	Concentration of water in bulk liquid (wt%)	71.5
17.	Tip concentration (wt%)	71.94
18.	Final temperature gradient (°C/cm)	
19.	Final tip concentration (wt%)	

Experiment: CAST mge Solidification Run 7

Hologram: 299

1.	Horizontal Image scale (pix/mm)	48
2.	Vertical Image scale (pix/mm)	60
3.	Column for carrier image (pix)	255
4.	Lower cutoff for carrier image (pix)	61
5.	Upper cutoff for carrier image (pix)	124
6.	Carrier frequency (pix)	91.51
7.	Column for experimental image (pix)	155
8.	Cuvette bottom for experimental image (pix)	480
9.	Interface for experimental image (pix)	302
10	Distance from right side of cuvette (pix)	648
11.	Lower cutoff for experimental image (pix)	40
12.	Upper cutoff for experimental image (pix)	161
13.	Fringe to fringe distance in FRINGE.PLT (pix)	26
14.	Maximum refractive index window in N.PLT (mm)	2.1
15.	Recommended temperature gradient (°C/cm)	16.33
16.	Concentration of water in bulk liquid (wt%)	71.5
17.	Tip concentration (wt%)	71.93
18.	Final temperature gradient (°C/cm)	
19.	Final tip concentration (wt%)	

Experiment: CAST mge Solidification Run 7

Hologram: 299

1.	Horizontal Image scale (pix/mm)	48
2.	Vertical Image scale (pix/mm)	60
3.	Column for carrier image (pix)	255
4.	Lower cutoff for carrier image (pix)	61
5.	Upper cutoff for carrier image (pix)	124
6.	Carrier frequency (pix)	91.51
7.	Column for experimental image (pix)	236
8.	Cuvette bottom for experimental image (pix)	480
9.	Interface for experimental image (pix)	301
10	Distance from right side of cuvette (pix)	240
11.	Lower cutoff for experimental image (pix)	30
12.	Upper cutoff for experimental image (pix)	138
13.	Fringe to fringe distance in FRINGE.PLT (pix)	23.25
14.	Maximum refractive index window in N.PLT (mm)	1.833
15.	Recommended temperature gradient (°C/cm)	18.26
16.	Concentration of water in bulk liquid (wt%)	71.5
17.	Tip concentration (wt%)	71.86
18.	Final temperature gradient (°C/cm)	
19.	Final tip concentration (wt%)	

Experiment: CAST mge Solidification Run 7

Hologram: 299

1.	Horizontal Image scale (pix/mm)	48
2.	Vertical Image scale (pix/mm)	60
3.	Column for carrier image (pix)	255
4.	Lower cutoff for carrier image (pix)	61
5.	Upper cutoff for carrier image (pix)	124
6.	Carrier frequency (pix)	91.51
7.	Column for experimental image (pix)	343
8.	Cuvette bottom for experimental image (pix)	480
9.	Interface for experimental image (pix)	313
10	Distance from right side of cuvette (pix)	133
11.	Lower cutoff for experimental image (pix)	52
12.	Upper cutoff for experimental image (pix)	137
13.	Fringe to fringe distance in FRINGE.PLT (pix)	22.67
14.	Maximum refractive index window in N.PLT (mm)	1.82
15.	Recommended temperature gradient (°C/cm)	18.73
16.	Concentration of water in bulk liquid (wt%)	71.5
17.	Tip concentration (wt%)	71.84
18.	Final temperature gradient (°C/cm)	
19.	Final tip concentration (wt%)	

Experiment: CAST mge Solidification Run 8

Hologram: 309

1.	Horizontal Image scale (pix/mm)	81.5
2.	Vertical Image scale (pix/mm)	101
3.	Column for carrier image (pix)	100
4.	Lower cutoff for carrier image (pix)	63
5.	Upper cutoff for carrier image (pix)	114
6.	Carrier frequency (pix)	91.0
7.	Column for experimental image (pix)	58
8.	Cuvette bottom for experimental image (pix)	480
9.	Interface for experimental image (pix)	312
10	Distance from right side of cuvette (pix)	426
11.	Lower cutoff for experimental image (pix)	34
12.	Upper cutoff for experimental image (pix)	143
13.	Fringe to fringe distance in FRINGE.PLT (pix)	30
14.	Maximum refractive index window in N.PLT (mm)	1.2
15.	Recommended temperature gradient (°C/cm)	23.82
16.	Concentration of water in bulk liquid (wt%)	71.5
17.	Tip concentration (wt%)	71.92
18.	Final temperature gradient (°C/cm)	
19.	Final tip concentration (wt%)	

Experiment: CAST mge Solidification Run 8

Hologram: 309

1.	Horizontal Image scale (pix/mm)	81.5
2.	Vertical Image scale (pix/mm)	101
3.	Column for carrier image (pix)	100
4.	Lower cutoff for carrier image (pix)	63
5.	Upper cutoff for carrier image (pix)	114
6.	Carrier frequency (pix)	91.0
7.	Column for experimental image (pix)	310
8.	Cuvette bottom for experimental image (pix)	480
9.	Interface for experimental image (pix)	303
10	Distance from right side of cuvette (pix)	574
11.	Lower cutoff for experimental image (pix)	44
12.	Upper cutoff for experimental image (pix)	133
13.	Fringe to fringe distance in FRINGE.PLT (pix)	30
14.	Maximum refractive index window in N.PLT (mm)	1.07
15.	Recommended temperature gradient (°C/cm)	23.82
16.	Concentration of water in bulk liquid (wt%)	71.5
17.	Tip concentration (wt%)	71.90
18.	Final temperature gradient (°C/cm)	
19.	Final tip concentration (wt%)	

Experiment: CAST mge Solidification Run 8

Hologram: 309

1.	Horizontal Image scale (pix/mm)	81.5
2.	Vertical Image scale (pix/mm)	101
3.	Column for carrier image (pix)	100
4.	Lower cutoff for carrier image (pix)	63
5.	Upper cutoff for carrier image (pix)	114
6.	Carrier frequency (pix)	91.0
7.	Column for experimental image (pix)	305
8.	Cuvette bottom for experimental image (pix)	480
9.	Interface for experimental image (pix)	306
10	Distance from right side of cuvette (pix)	1015
11.	Lower cutoff for experimental image (pix)	48
12.	Upper cutoff for experimental image (pix)	135
13.	Fringe to fringe distance in FRINGE.PLT (pix)	32
14.	Maximum refractive index window in N.PLT (mm)	0.91
15.	Recommended temperature gradient (°C/cm)	22.33
16.	Concentration of water in bulk liquid (wt%)	71.5
17.	Tip concentration (wt%)	71.79
18.	Final temperature gradient (°C/cm)	
19.	Final tip concentration (wt%)	

Experiment: CAST mge Solidification Run 8

Hologram: 310

1.	Horizontal Image scale (pix/mm)	81.5
2.	Vertical Image scale (pix/mm)	101
3.	Column for carrier image (pix)	200
4.	Lower cutoff for carrier image (pix)	79
5.	Upper cutoff for carrier image (pix)	119
6.	Carrier frequency (pix)	106.97
7.	Column for experimental image (pix)	244
8.	Cuvette bottom for experimental image (pix)	480
9.	Interface for experimental image (pix)	319
10	Distance from right side of cuvette (pix)	232
11.	Lower cutoff for experimental image (pix)	60
12.	Upper cutoff for experimental image (pix)	158
13.	Fringe to fringe distance in FRINGE.PLT (pix)	35.5
14.	Maximum refractive index window in N.PLT (mm)	1.0
15.	Recommended temperature gradient (°C/cm)	20.13
16.	Concentration of water in bulk liquid (wt%)	71.5
17.	Tip concentration (wt%)	71.77
18.	Final temperature gradient (°C/cm)	
19.	Final tip concentration (wt%)	

Experiment: CAST mge Solidification Run 8

Hologram: 310

1.	Horizontal Image scale (pix/mm)	81.5
2.	Vertical Image scale (pix/mm)	101
3.	Column for carrier image (pix)	200
4.	Lower cutoff for carrier image (pix)	79
5.	Upper cutoff for carrier image (pix)	119
6.	Carrier frequency (pix)	106.97
7.	Column for experimental image (pix)	234
8.	Cuvette bottom for experimental image (pix)	480
9.	Interface for experimental image (pix)	274
10	Distance from right side of cuvette (pix)	690
11.	Lower cutoff for experimental image (pix)	60
12.	Upper cutoff for experimental image (pix)	164
13.	Fringe to fringe distance in FRINGE.PLT (pix)	35
14.	Maximum refractive index window in N.PLT (mm)	1.07
15.	Recommended temperature gradient (°C/cm)	20.42
16.	Concentration of water in bulk liquid (wt%)	71.5
17.	Tip concentration (wt%)	71.80
18.	Final temperature gradient (°C/cm)	
19.	Final tip concentration (wt%)	

Experiment: CAST mge Solidification Run 8

Hologram: 310

1.	Horizontal Image scale (pix/mm)	81.5
2.	Vertical Image scale (pix/mm)	101
3.	Column for carrier image (pix)	200
4.	Lower cutoff for carrier image (pix)	79
5.	Upper cutoff for carrier image (pix)	119
6.	Carrier frequency (pix)	106.97
7.	Column for experimental image (pix)	271
8.	Cuvette bottom for experimental image (pix)	480
9.	Interface for experimental image (pix)	319
10	Distance from right side of cuvette (pix)	1079
11.	Lower cutoff for experimental image (pix)	65
12.	Upper cutoff for experimental image (pix)	160
13.	Fringe to fringe distance in FRINGE.PLT (pix)	39
14.	Maximum refractive index window in N.PLT (mm)	1.01
15.	Recommended temperature gradient (°C/cm)	18.32
16.	Concentration of water in bulk liquid (wt%)	71.5
17.	Tip concentration (wt%)	71.75
18.	Final temperature gradient (°C/cm)	
19.	Final tip concentration (wt%)	

VITA

Brent William Blaha was born on March 18, 1969 in Bethesda, Maryland. As the son of a career naval officer, he has lived in numerous areas up and down the East Coast, as far north as New Hampshire and as far south as Mississippi. His family remained in Virginia Beach, Virginia, long enough for him to attend and graduate from Kempsville High School in 1987. In that same year, he began studies at the University of Virginia in Charlottesville for which he was awarded a Bachelor of Science degree in Aerospace Engineering in the spring of 1991. Pursuing higher education at the Univeristy of Tennessee Space Institute in the fall of that year, he accepted a graduate research assistantship with the Center for Laser Applications in January, 1992; and received a NASA Graduate Student Researcher's Program Fellowship the following August. He received a Master of Science degree in Mechanical Engineering in May, 1994.

Mr. Blaha is a member of the American Institute of Aeronautics and Astronautics and Theta Chi fraternity. He continues work towards a Doctor of Philosophy degree in Mechanical Engineering.